

# X-ray annual modulation observed by XMM-Newton and Axion Quark Nugget Dark Matter

Shuailiang Ge<sup>a,b</sup>, Hikari Rachmat<sup>b</sup>, Md Shahriar Rahim Siddiqui<sup>b</sup>, Ludovic Van Waerbeke<sup>b</sup>, Ariel Zhitnitsky<sup>b</sup>

<sup>a</sup>Center for High Energy Physics, Peking University, Beijing 100871, China

<sup>b</sup>Department of Physics and Astronomy, University of British Columbia, Vancouver, V6T 1Z1, BC, Canada

---

## Abstract

The XMM-Newton observatory shows evidence, with a  $11\sigma$  confidence level, for seasonal variation of the X-ray background in the near-Earth environment in the 2-6 keV energy range [1]. The authors argue that the observed seasonal variation suggests a possible link with dark matter. We propose an explanation which involves the Axion Quark Nugget (AQN) dark matter model. In our proposal, AQNs can cross the Earth and emit high energy photons at their exit. We show that the emitted spectrum is consistent with [1], and that our calculation is not sensitive to the specific details of the model. Our proposal predicts a large seasonal variation, on the level of 20-25%, much larger than conventional dark matter models (1-10%). Since the AQN emission spectrum extends up to  $\sim 100$  keV, well beyond the keV sensitivity of XMM-Newton, we predict the AQN contribution to the hard X-ray and  $\gamma$ -ray backgrounds in the Earth's environment. The Gamma-Ray Burst Monitor (GBM) instrument, aboard the FERMI telescope, is sensitive to the 8 keV-40 MeV energy band. The NuSTAR (Nuclear Spectroscopic Telescope Array) is a NASA space based X ray telescope which operates in the range 3 to 79 keV is also sensitive to higher energy bands. We suggest that the multi-year archival data from the GBM or NuSTAR could be used to search for a seasonal variation in the near-Earth environment up to 100 keV as a future test of the AQN framework.

*Keywords:* Axion, Dark Matter, X-ray

---

## 1. Introduction

The near-Earth Cosmic X-Ray Background (CXB) has been recently measured by [1] using archived data from the X-ray XMM-Newton telescope. After a big effort to remove the instrumental background and the constant cosmic background, they discovered a seasonal variation of a strong CXB residual, with a confidence level of  $11\sigma$  in the 2-6 keV energy band (see Fig. 14 of [1]). Moreover, the amplitude of the variation is an order one effect with the signal. If this CXB residual was coming from unresolved

---

*Email address:* sge@pku.edu.cn (Shuailiang Ge)

extragalactic sources, we would expect it to be uniform and not varying with seasons. The fact that there is an order one effect correlated with the relative positions of the Sun and Earth is unexpected and it suggests a local, near Earth and/or Sun, cause. As a result, the authors of [1] searched for a possible explanation outside of the conventional astrophysical paradigm, after excluding other instrumental possibilities.

The authors of [1] propose an explanation based on the assumption that keV axions are emitted by the Sun and convert to X-rays in the Earth's magnetosphere. These X-rays would be subsequently elastically scattered, on average, through a right angle towards the XMM-Newton telescope. Note that an even earlier idea was proposed by [2, 3, 4] which views the axion-emitting solar core through the solid Earth with an X-ray telescope. The original idea by [2] cannot explain the effect found by [1] because the XMM-Newton's operations exclude pointing at the Sun and at the Earth directly. Some of the major criticism of the [1] interpretation include the following [5]: a) Due to conservation of momentum, in conventional cases, the X-ray photons generated in the magnetic field should be collinear with the parent axions. Therefore, since XMM-Newton never directly points towards the Sun, it should not see any solar axions; b) Only in the case of a highly inhomogeneous component of the magnetic field with a fluctuation in the keV scale would the photons be non-collinear with the parent axions. Such a fast fluctuating component is very unlikely to be a dominant portion of a geomagnetic field. Even if non-collinear effects are generated in the geomagnetic field and we assume that the photon flux converted from axions would be totally isotropic, the geometric factor  $\xi = \Omega_{\text{XMM}}/4\pi$  (where  $\Omega_{\text{XMM}}$  is the aperture of XMM-Newton) is very small,  $\xi \simeq 10^{-5}$ . This is in strong disagreement with the requirement of  $\xi \simeq 1$  for the interpretation of the observed seasonal variation as proposed by [1]. Other issues with this interpretation were also discussed in [5].

The main goal of the present work is to offer an alternative explanation for the observed seasonal variation [1] which does not suffer the fundamental problems mentioned above. Before we discuss our proposal, we would like to make few comments about [1] in relation to previous studies on the CXB. It is important to point out that the data set used by [1] is perfectly consistent with all previous measurements of CXB when averaged over all seasons. The novelty here is the seasonal variation. The fact that it is an order of one effect is very unexpected, because it is normally assumed that the isotropic CXB residual is related to unresolved extra-galactic point sources, therefore uncorrelated with the positions of the Sun or Earth. In this sense the claim by [1] on observation of the seasonal variations is hard to reconcile with claim of ref. [6] that the X ray background measurements in (2-10) keV band could be interpreted that the CHANDRA observations have resolved (70-90)% of the background into discrete sources. Our view here is that there could be some loopholes with this interpretation, the topic which is obviously well beyond the scope of the present work. In what follows, we assume that the seasonal variations indeed had been observed and properly measured by [1].

Although the explanation given by [1] turns out to be untenable, the phenomenon of a seasonally varying X-ray background around the Earth detected with an  $11\sigma$  confidence level remains a mystery (see Fig. 1). The seasonal variation pattern is clearly related to the Earth's revolution around the Sun, which strongly indicates that dark matter galactic wind could play a central role. In the present work we propose that the

observed seasonally varying X-ray background could be a result of the annually modulating dark matter wind in the context of the Axion Quark Nugget (AQN) dark matter model [7]. In our framework, the AQNs emit X-rays isotropically and can propagate in any directions. The radiated X-rays are automatically subject to seasonal variations, since the AQNs are the dominant contributor to dark matter in this framework. Our proposal is therefore very different from [2, 3, 4, 1] which consider axions as the dominant source of dark matter. More importantly, in our proposal the emitted X rays do not scatter through a right angle to reach the telescope, which is the weakest and physically unjustified assumption of the explanation proposed by [1].

The AQN model was initially proposed to explain why dark matter and visible matter densities assume similar magnitudes,  $\Omega_{\text{DM}} \sim \Omega_{\text{visible}}$ . The basic features of the model will be reviewed in section 2, but at its heart lies the existence of antimatter nuggets which can interact strongly with regular matter. Remarkably, the antimatter dark matter formulated in the model does not lead to contradictions with known observations. It is quite the contrary; it leads to a series of observational signatures that could explain several outstanding astrophysical puzzles. A non-exhaustive list includes the ‘‘Primordial Lithium Puzzle’’ [8], ‘‘The Solar Corona Mystery’’ [9, 10], the recent EDGES observations [11], and the annual modulation observed by the DAMA/LIBRA experiment<sup>1</sup>. In the center of the Milky Way, the interaction between antimatter AQNs and baryonic matter also leads to electromagnetic signatures which could explain various emission excesses in different frequency bands, such as the well known 511 keV line [15, 16] and mysterious diffuse UV radiation [17].

The basic idea in our proposal follows from the fact that antimatter AQNs hit the Earth at a low rate. These AQNs will lose some of their mass from annihilation, and they will also lose some momentum [18]. The nuggets are not completely destroyed. At the moment of their exit, they are very hot objects as a result of friction and annihilation events occurring in the Earth’s deep underground layers. At the exit point, their temperature can be as high as  $T_0 \sim 200$  keV (this is discussed in Section 3). The AQNs slowly cool down while they continue their trajectory away from the Earth’s surface and emit radiation. At this stage, the AQNs continue to lose their accumulated heat and slowly decrease their internal temperature. On average, when AQNs reach distances of the order  $r \gtrsim 8R_{\oplus}$ , their temperature remains very high,  $T \gg 10$  keV. The *XMM-Newton* operates precisely at such distance and can easily observe these X-rays emitted by AQNs. AQNs represent the dominant form of dark matter in this model, and the velocities of AQNs hitting the Earth are different for different seasons. We call this the annual modulation of the dark matter wind (see footnote 2 for a comment on this terminology). As a result, the flux of AQNs that leave the Earth also depends on seasons, which consequently leads to a seasonal varying X-ray background. Ideally, our model should match the observed seasonal variation shown in Fig. 1. This can only be done with the knowledge of the telescope orientation and position changes as a

---

<sup>1</sup>The DAMA/LIBRA (DL) experiment [12, 13] claims an observation of an annual modulation in the 1-6 keV recoil energy range with a  $9.5\sigma$  confidence level, strongly suggesting that the observed modulation has a dark matter origin. However, the conventional interpretation in terms of WIMP-nucleon interaction is excluded by other experiments. The AQN framework offers an alternative source of modulation observed by DL in the form of neutrons which have been liberated from surrounding material [14].

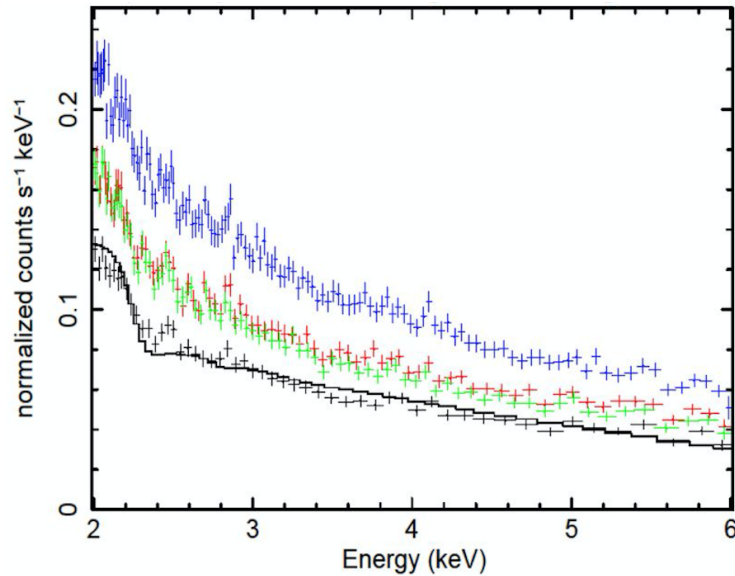


Figure 1: 2-6 keV X-ray background spectra detected by the EPIC pn camera carried by *XMM-Newton* (the data are integrated from 2000 to 2012) for each of the four spacecraft seasons: Winter (black), Summer (green), Spring (red), and Fall (blue). The solid black line corresponds to the fit (27) for Winter season. The plot is adopted from Figure 14(a) in [1].

function of seasons, information we do not have. For this reason, a precise comparison with observations cannot be done at this time<sup>2</sup>, and future observations are required to calculate a precise X ray seasonal variation consistent with the telescope orientations and positions changes over time. However, we will show that our model can reproduce the amplitude of the seasonal variations, which is on the level of 20-25% (see Fig. 1), and the energy spectrum measured in [1].

The paper is organized as follows. In Section 2, we briefly review the AQN model. In Section 3, we calculate the thermal emission spectrum of a single AQN and its cooling process in space after it leaves the Earth. In Section 4, we calculate the total spectrum received by *XMM-Newton* from AQNs that enter the field of view of the telescope, and compare it with the observations. In Section 5, we calculate the seasonal variation of the AQN-induced spectrum. Finally, we conclude the main points of this work in Section 6.

<sup>2</sup>There are subtle points here related to *XMM-Newton*'s position and its view angle as it orbits the Earth. This complication does not allow an immediate interpretation of the data in terms of the conventional annual modulation, which is normally attributed to dark matter wind with its maximum on June 1 and minimum on Dec 1. See the original paper by [19] and review [20] for more information. The maximum and minimum values will obviously get shifted as a function of the satellite's position with respect to the Earth's surface. We will make a few comments on these complications later in the text.

## 2. The AQN model

In this model, dark matter consists of axion quark nuggets (AQNs) which are macroscopically large objects of nuclear density with a typical size of  $R \sim 10^{-5}$  cm and typical mass of  $B \sim 10^{25}$  times the mass of a proton.  $B$  is also called the baryonic charge. AQNs are dense objects made of standard model quarks and gluons in the colour superconducting (CS) phase [7]. This model is conceptually similar to the original nuclearites proposed by [21], where these nuggets are “cosmologically dark” not through the weakness of their interactions but due to their small cross-section to mass ratio. As a result, the corresponding constraints on this type of dark matter place a lower bound on their mass, rather than their coupling constant.

The presence of a large amount of antimatter in the form of high density AQNs leads to many observable consequences as a result of very rare annihilation events between antiquarks in AQNs and baryons in the visible Universe.

It is normally assumed that the Universe started in a neutral phase with zero baryonic charge, then it evolved into a state with a net positive baryon number through a “baryogenesis” process. In the AQN model, the “baryogenesis” is replaced by the *charge separation process* in which the total baryon charge of the Universe remains zero at all times. However, due to the global  $\mathcal{CP}$  violating processes associated with the axion’s potential misalignment angle  $\theta_0 \neq 0$  during the early formation stage at the QCD scale, the number and size distributions of nuggets and antinuggets will necessarily be different by an order of one. This happens regardless of the axion mass  $m_a$  and the initial value of  $\theta_0$ . We refer the readers to some original work for a detailed analysis on the formation of nuggets [22], the development of nugget-antinugget asymmetry [23, 24], and their size distribution and survival pattern [25] in the unfriendly environment of the early Universe, see also a brief recent review [26] covering these topics.

In the AQN model, dark matter will emit radiation when it collides with visible baryons as a result of annihilation processes. Because of the AQN’s low number density, this is a very rare event. It is surprising at first that a model with dark matter in form of the antimatter nuggets could even pass the simplest observational constraint, but the reason lies in the fact that most of a nugget’s mass is inside the nugget and does not contribute to the emission processes. A comparison of the emission mechanisms to astrophysical observations from radio to  $\gamma$ -ray wavelengths suggests that the nugget’s mass should have a baryon charge of  $\langle B \rangle > 10^{24}$  to avoid the overproduction of the observed galactic diffuse background and be consistent with all known observations. This corresponds to an AQN mass of only  $\sim 1$  gram, therefore AQNs of mass  $\sim 1$  gram and higher are viable dark matter candidates. As mentioned in the Introduction, there are several excesses of emissions in different frequency bands contained in the galactic spectrum, which seem to be consistent with the moderate emission processes inherent to the AQN model.

The X-ray emission in the near-Earth environment, which is the subject of our present work, is originated from the electrosphere of the nugget. Therefore the thermal properties of the electrosphere plays a crucial role. The relevant thermal features of the electrosphere have been analyzed previously in [27] in the context of galactic emission, where the nugget’s internal temperature turns out to be very low, being around  $T \sim \text{eV}$ . due to the very low density of the environment on the level  $n_B \sim 10^2 \text{cm}^{-3}$ . In our

present study, we are interested in the nuggets crossing the Earth's interior with a very high density of the surrounding material, around  $n_B \sim 10^{24} \text{cm}^{-3}$ , and even higher in the Earth's core. As a result, the nuggets crossing the Earth's interior will acquire very high temperatures, reaching up to  $T \simeq 200 \text{ keV}$ , as estimated in the next section. For such high temperatures, several new phenomena related to ionization, plasma frequency, and other many-body effects, which had been previously neglected in [27], become very important and have to be explicitly incorporated into the computational framework. The corresponding modifications of the dynamics of the electrosphere accounting for all of these effects will be the subject of the following Section 3. We use these results in Section 4 to calculate the spectrum accumulated by XMM-Newton from the hot AQNs based on the observatory's configuration and orbit information, and compare it with the observations.

### 3. AQN-induced x-rays

In order to theoretically calculate the spectrum received by XMM-Newton from the radiation of hot AQNs that have crossed the Earth's interior, the first step is to know the radiation spectrum from the electrosphere of an AQN characterized by a high temperature  $T \simeq 200 \text{ keV}$ , which represents the topic of subsection 3.1. In subsection 3.2, we examine the cooling process of AQNs in space after they leave the Earth. Since the AQN's radiation features change as its temperature drops, we need to know the temperature, intensity, and spectrum of AQNs when they reach the region  $r \sim 10R_\oplus$ , where the XMM-Newton is operational.

#### 3.1. AQN emissivity

The properties of thermal emission from the electrosphere of a nugget have been discussed in [27]. The process of radiation is Bremsstrahlung emission when the positrons scatter and emit photons with typical energy  $\sim T$ . First, we will briefly summarize the previous results here. Next, we will discuss a number of complications which are relevant for our present work (when the temperature is very high  $T \simeq 200\text{-}500 \text{ keV}$ ). These were ignored in previous studies with  $T \simeq \text{eV}$  in the context of galactic emission.

The spectral surface emissivity is denoted as  $dF/d\omega = dE/dtdAd\omega$ , representing the energy emitted by a single nugget per unit time, per unit area of the nugget's surface, and per unit frequency. It has the following expression [27]:

$$\frac{dF}{d\omega} = \frac{1}{2} \int_0^\infty dz \frac{dQ}{d\omega}(\omega, z), \quad F_{\text{tot}}(T) \equiv \int_0^\infty \frac{dF}{d\omega} d\omega \simeq \frac{16}{3} \frac{T^4 \alpha^{5/2}}{\pi} \sqrt[4]{\frac{T}{m}}, \quad (1)$$

where

$$\frac{dQ}{d\omega} = n^2(z) \cdot \frac{4\alpha}{15} \left( \frac{\alpha}{m_e} \right)^2 2\sqrt{\frac{2T}{m_e \pi}} \left( 1 + \frac{\omega}{T} \right) e^{-\omega/T} h\left(\frac{\omega}{T}\right). \quad (2)$$

$n(z)$  is the local density of positrons at distance  $z$  from the nugget's surface, which has the following expression

$$n(z) = \frac{T}{2\pi\alpha} \frac{1}{(z + \bar{z})^2}, \quad (3)$$

with

$$\bar{z}^{-1} = \sqrt{2\pi\alpha} \cdot m_e \cdot \left(\frac{T}{m_e}\right)^{1/4}, \quad n(z=0) \simeq (m_e T)^{3/2}, \quad (4)$$

where  $n(z=0)$  reproduces an approximate formula for the plasma density in the Boltzmann regime at temperature,  $T$ . The parameter  $\bar{z}$  was introduced in [27] as a constant of integration and has the dimension of a length scale where the Boltzmann regime is realized. The function  $h(x)$  in Eq. (2) is a dimensionless function computed in [27] (see Appendix A for details). The important features of the spectrum will be discussed in detail at the end of this subsection, but we would like to emphasize that it is qualitatively different from conventional black body radiation, despite of the fact that the electrosphere is characterized by a specific temperature,  $T$ . The reason is that the size of the system is much smaller than the photon's mean free path and, as a result, the photons cannot thermalize in this system. The resulting spectrum is very broad and extends to the energies much lower than the temperature  $T$ , in contrast with black body radiation.

A typical internal temperature  $T$  of the nuggets can be estimated from the condition that the radiative output of equation (1) must be balanced by the flux of energy onto the nugget due to the annihilation events. In this case we may write,

$$F_{\text{tot}}(T) \cdot (4\pi R^2) \simeq \bar{\kappa} \cdot (\pi R^2) \cdot (2 \text{ GeV}) \cdot n_{\text{out}} \cdot v_{\text{AQN}}, \quad (5)$$

where the left hand side accounts for the total energy radiation from the nuggets' surface per unit time as given by (1), while the right hand side accounts for the rate of annihilation events when each successful annihilation event of a single baryon charge produces  $\sim 2m_p c^2 \simeq 2 \text{ GeV}$  energy. In (5) we assume that the nugget is characterized by the geometrical cross section  $\pi R^2$  when it propagates in environment with local density  $n_{\text{out}}$  with velocity  $v_{\text{AQN}} \sim 10^{-3}c$ .

The factor  $\bar{\kappa}$  is introduced to account for the fact that not all matter striking the nugget will annihilate and not all of the energy released by an annihilation will be thermalized in the nuggets. In a neutral dilute environment considered previously [27] the value of  $\bar{\kappa}$  cannot exceed  $\bar{\kappa} \lesssim 1$  which would correspond to the total annihilation of all impacting matter into thermal photons. The high probability of reflection at the sharp quark matter surface lowers the value of  $\bar{\kappa}$ . The propagation of an ionized (negatively charged) nugget in a highly ionized plasma (such as solar corona) will increase the effective cross section. As a consequence, the value of  $\bar{\kappa}$  could be very large as discussed in [10] in application to the solar corona heating problem.

The thermal properties presented above were applied to the study of the emission from AQNs from the Galactic Centre, where a nugget's internal temperature is very low,  $T \sim \text{eV}$ , as already mentioned in Section 2. When the nuggets propagate in the Earth's atmosphere, the AQN's internal temperature starts to rise up to  $\sim 20 \text{ keV}$  or so. When the AQN enters the Earth's surface, it further heats up to  $\sim 200 \text{ keV}$ , due to the much higher density of the Earth's interior. Indeed, from (1) and (5) one can estimate

the internal temperatures in atmosphere and in the Earth's interior as follows:

$$\begin{aligned} T_{\text{atmosphere}} &\sim 15 \text{ keV} \cdot \left( \frac{n_{\text{atmosphere}}}{3 \cdot 10^{20} \text{ cm}^{-3}} \right)^{\frac{4}{17}} \left( \frac{\bar{\kappa}}{0.1} \right)^{\frac{4}{17}}, \\ T_{\text{interior}} &\sim 200 \text{ keV} \cdot \left( \frac{n_{\text{interior}}}{10^{25} \text{ cm}^{-3}} \right)^{\frac{4}{17}} \left( \frac{\bar{\kappa}}{0.1} \right)^{\frac{4}{17}}, \end{aligned} \quad (6)$$

where the temperature  $T \sim 15 \text{ keV}$  had been used previously in [28] for the AQN propagating under thunderclouds to explain the unusual Cosmic Ray like events observed by Telescope Array Collaboration, while  $T \sim 200 \text{ keV}$  had been used in [29] to explain unusual clustering events observed by the HORIZON -10T collaboration. In what follows, we use  $T_0 \approx 200 \text{ keV}$  as the benchmark temperature for the nuggets exiting the Earth's surface. However, as we explain in next subsection a precise computations of  $T_0$  from the first principles is a very difficult problem. Therefore, we opted to keep  $T_0$  as the phenomenological parameter, which will be determined by observational constraints.

While the nuggets propagate underground, the heat from the electrosphere is transferred to the nugget's core, accompanied by the emission of photons with a spectrum characterized by Eq. (1). These processes are very complicated to compute because in this temperature regime, a number of many-body effects in the electrosphere, that were previously ignored, become important. In what follows, we explain the physics of these effects, while all of the technical details are developed in Appendix A.

#### 1. *The modification of the positron's density $n(z)$ in the electrosphere*

The most important modification due to high temperature occurs as a result of the ionization of the system. Loosely bound positrons leave the system, and strongly bound positrons change their positions and momenta to adjust to the corresponding modifications of the system. Indeed, the neutrality of the AQN will be lost due to the ionization at  $T \neq 0$ , in which case the antimatter nuggets will acquire a negative electric charge due to the ionized positrons.

Since the temperature of the AQN's core becomes very high due to the large number of annihilation events in the Earth's interior, a large number of weakly bound positrons will be stripped off of the nugget, and the number density of remaining positrons will drastically decrease. The corresponding changes in the electrosphere are determined by nontrivial non-equilibrium dynamics, which shall not be discussed in the present work. Instead, we introduce a phenomenological suppression factor,  $\kappa \ll 1$ , not to be confused with parameter  $\bar{\kappa}$  introduced earlier, which effectively accounts for the relevant physics:

$$n(z) = \kappa \cdot \frac{T}{2\pi\alpha} \frac{1}{(z + \bar{z})^2}. \quad (7)$$

Although the precise computations of the coefficient  $\kappa \ll 1$  from first principles is not possible at this stage, a simple estimate based on simple assumptions will be given below. The estimate suggest that  $\kappa \sim 10^{-3}$  as a result of dramatic expansion of the electrosphere at high temperatures, in which case the effective density of the positrons (7) will be dramatically diminish.

Eq. (7) is a simplification which does not take into account the fact that loosely bound positrons will be completely stripped off by high temperature, while more strongly



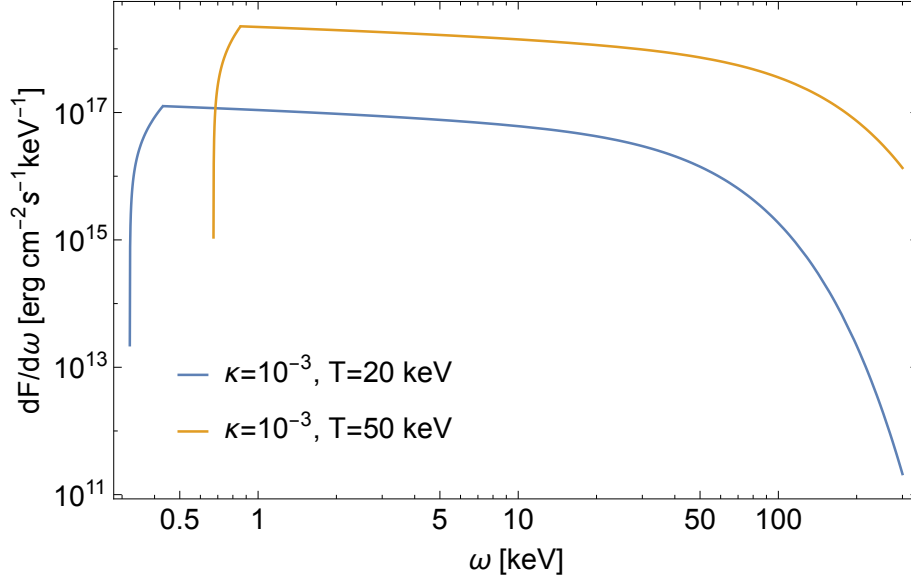


Figure 2: The spectral surface emissivity of a nugget with all of the effects discussed in this subsection included, see (A.8) in Appendix Appendix A. This is plotted for  $\kappa = 10^{-3}$  with  $T = 20$  keV and 50 keV respectively, for illustrative purpose.

bound positrons will be less affected and stay bound. One can easily add this feature to our simplified analysis by describing  $\kappa$  as a step function:

$$\kappa(z, T) = \begin{cases} 0 & \text{if } z \geq z_1 \\ \kappa(T) & \text{if } z < z_1 \end{cases}, \quad (8)$$

where  $z_1(T)$  is defined as

$$z_1(T) \simeq \frac{1}{\sqrt{2m_e T}}. \quad (9)$$

In this way, we preserve the crucial feature of the system that loosely bound positrons from the outer region of the electrosphere are stripped from the nugget and do not participate in the cooling of the system.

### 2. The role of the plasma frequency

The plasma frequency  $\omega_p$  characterizes the propagation of photons in a plasma. It can be thought of as an effective mass for the photons: only photons with an energy larger than this mass can propagate outside of the system, while photons with  $\omega < \omega_p$  can only propagate for a short time and distance  $\sim \omega_p^{-1}$  before being absorbed back. For our estimates, we will use a conventional non-relativistic expression for  $\omega_p$ :

$$\omega_p^2(z) = \frac{4\pi\alpha n(z)}{m_e}; \quad \omega_p(z) \simeq \sqrt{\frac{2T}{m_e}} \frac{\sqrt{\kappa}}{(z + \bar{z})}, \quad (10)$$

where we substituted Eq. (7).

The important implication of the plasma frequency  $\omega_p(z)$  is that the densest regions of the electrosphere stop emitting photons because the plasma frequency is too high, since  $\omega_p^2 \sim n$  according to (10). This implies that the emissivity (Eq. (2)) from the dense regions will be exponentially suppressed at the plasma frequency [27]:

$$\frac{d\tilde{Q}}{d\omega}(\omega, z) \sim e^{-\omega_p(z)/T} \cdot \frac{dQ}{d\omega}(\omega, z). \quad (11)$$

With all of these effects taken into account, the spectral surface emissivity (1) can now be numerically computed. We refer the reader to Appendix A for technical details of the computations. Two examples are shown in Fig. 2 with  $\kappa(T) = 10^{-3}$ ,  $T = 20$  keV and  $\kappa(T) = 10^{-3}$ ,  $T = 50$  keV respectively, for illustrative purpose. Fig. 2 reveals some important features. First of all, the spectrum is almost flat in the region  $\omega \lesssim T$ . This is a direct manifestation of a very generic property of emission by charged particles when the energy of the emitted photon is much smaller than all of the other scales of the problem, the so-called “soft Bremsstrahlung” emission or “soft photon theorem.” In this case, the emission is known to show a  $d\omega/\omega$  behaviour for the probability to emit a soft photon with frequency  $\omega$ . This property implies that the intensity of radiation,  $dF/d\omega \sim \text{constant}$ , must be flat for soft photons. As we will discuss in Section 4, this unique property of the spectrum will play a key role in our interpretation of the spectrum observed by XMM-Newton. On the other hand, for large  $\omega \gg T$ , the exponential suppression,  $\exp(-\omega/T)$ , becomes the most important feature of the spectrum. The complete suppression of the emission at very small  $\omega \ll T$  is an artifact of our simplification of the density,  $n(z) \sim \kappa(z)$ , in form of a step function (8). There is another cusp behaviour also at  $\omega \ll T$  (peak on Fig. 2). This results from our simplified treatment of the plasma frequency,  $\omega_p$ , when the  $dF/d\omega$  is approximated by a piecewise function (when the emission with  $\omega \geq \omega_p$  from a high density region occurs with no suppression, while emission with  $\omega \leq \omega_p$  from the same region is completely dropped). In reality, both of these effects leading to the cusps should be described by a smooth function. However, this part of the spectrum with  $\omega \ll T$  will not play any role in our analysis which follows<sup>3</sup>.

The next step is the computation of the cooling rate, done in subsection 3.2. For this purpose, we need the total surface emissivity,  $F_{\text{tot}}(T, \kappa)$ , as a function of  $T$  and  $\kappa$ . This is done by numerically integrating  $dF/d\omega$  over  $\omega$ . The difference in comparison with simple analytical formula given in (1) is that the expression below accounts for all additional effects discussed in this subsection. The technical details of the calculations can be found in Appendix A, Eq. (A.13). We parameterize the final formula for the emissivity, which will be used in subsection 3.2 to study the AQN’s cooling, as follows:

$$F_{\text{tot}}(T) \simeq \frac{\alpha}{15\pi^{5/2}} \frac{T^5}{m_e} \cdot c_1(\kappa) \left( \frac{T}{10 \text{ keV}} \right)^{c_2(\kappa)} \quad (12)$$

---

<sup>3</sup>An important consequence of the strong suppression at small  $\omega \ll T$  is that the intensity of the visible light emission with  $\omega \sim 1$  eV is strongly suppressed in comparison to the X-ray emission. It could play a dramatic role in the identification of AQN annihilation events in the atmosphere with the so-called skyquakes. They occur when a sonic boom is not accompanied by any visible light, which would normally be expected for any meteors-like events, see [30] for details.

with

$$c_1(\kappa) = 4\kappa^2, \quad c_2(\kappa) = -0.89. \quad (13)$$

### 3.2. AQN cooling

While passing through the Earth, nuggets will heat up by friction and annihilation events. Their temperature when exiting the Earth's surface is denoted by  $T_0$ , and it assumes the value  $T_0 \sim 200$  keV as estimated in (6). While traversing the Earth, the nugget will heat up in a fraction of a second because of the very efficient energy transfer between the nugget and its surrounding dense material. However, it is expected that  $T_0$  cannot become higher than  $\sim 500$  keV because of different processes. These include  $e^+e^-$  pair production and black body radiation, which start to dominate the nugget's emission deep underground, and become much more important than the Bremsstrahlung radiation (2). Calculating  $T_0$  precisely from first principles remains very difficult because the energy transfer in the Earth's interior includes complicated processes, such as turbulence and acoustic shock waves with a very large Mach number,  $M$ .  $M = v_{\text{AQN}}/c_s \gg 10$ , where  $c_s$  is the speed of sound of the surrounding material. This part of the nugget's physics is very complicated, and it is not part of our present work. For this reason, we will treat  $T_0$  as a phenomenological parameter, which we expect to be close to  $T_0 \simeq 200$  keV, as mentioned above. However, for illustrative purposes we also present the results for  $T_0 \simeq 500$  keV.

Fortunately, these complications do not affect our analysis once the AQNs exit the surface and start to travel in empty space. After exiting Earth, the energy loss from the AQN into space is entirely determined by Eq. (12). In this case, the initial condition for the cooling is simply characterized by  $T_0$ . One can completely ignore any new annihilation events at this point because the density of the material in Earth's atmosphere drops very quickly with height. Therefore, the nuggets are assumed to be travelling in empty space immediately after they exit the Earth's surface, with initial temperature  $T(r = R_\oplus) = T_0$ .

Our goal now is to calculate the energy loss rate of the heated AQN while it travels through space, away from Earth, with a typical dark matter speed of  $\sim 220$  km/s. The total initial energy accumulated by the AQN is determined by its exit temperature,  $T_0$ , and specific heat,  $c_V$ . There are many different CS phases with drastically different expressions for  $c_V$ . In particular, in 2SC (two flavour superconducting phase), the expression for the specific heat assumes the form [31]:

$$c_V \simeq \frac{1}{3}T(\mu_d^2 + \mu_u^2), \quad (14)$$

where chemical potentials in CS phases are in the range  $\mu_u \simeq \mu_d \simeq 500$  MeV. This numerical value is perfectly consistent with our studies of the typical value of the AQN's chemical potential at the moment of its formation [25]. For our numerical analysis in what follows, we use expression (14).

The energy of the nugget decreases when its temperature decreases, according to the conventional formula

$$dE = c_V \cdot V \cdot dT, \quad (15)$$

where  $V$  is the AQN's volume. The energy emitted by a nugget per unit time has been computed in the previous section and it is given by (12):

$$-dE/dt = F_{\text{tot}}(T) \cdot 4\pi R^2, \quad (16)$$

where sign minus implies that the energy of the AQN is decreasing with time as a result of emission. Combining (15) and (16), we arrive at the desired equation describing the change of the temperature,  $T$ , with time,  $t$ , while the AQN is moving away from the Earth and emitting photons:

$$\frac{dT}{dt} = -\frac{4\pi R^2}{V} \frac{1}{c_V(T)} F_{\text{tot}}(T). \quad (17)$$

The solution of this differential equation, with initial condition  $T(t = 0) = T_0$ , is given by:

$$\left(\frac{t}{1 \text{ sec}}\right) \simeq \frac{0.34}{c_1(\kappa)[c_2(\kappa) + 3]} \left(\frac{R}{10^{-5} \text{ cm}}\right) \left(\frac{\mu_{u,d}}{500 \text{ MeV}}\right)^2 \cdot \left[ \left(\frac{T}{10 \text{ keV}}\right)^{-[c_2(\kappa)+3]} - \left(\frac{T_0}{10 \text{ keV}}\right)^{-[c_2(\kappa)+3]} \right], \quad (18)$$

where  $T(t) = T_0$  at  $t = 0$ , when the nugget exits the Earth's surface. We refer the readers to Appendix Appendix B for the details on the derivation.

Fig. 3 shows  $T$  as a function of time,  $t$ , for different values of  $\kappa$  and  $T_0$ . We choose  $R = 2.25 \cdot 10^{-5} \text{ cm}$ , which has been previously used in axion emission studies [18]. Fig. 3 illustrates a very important result: after  $t \approx 100$  seconds, when the AQN is at distance  $r \geq 3R_\oplus$ , the temperature  $T(t)$  is not very sensitive to the initial temperature  $T_0$  for a given coefficient  $\kappa$ . This is because AQNs with higher initial temperature  $T_0$  emit more radiation and cool down more quickly. As a result,  $T(t)$  is much more sensitive to  $\kappa$  than  $T_0$ , as shown by the blue and black lines in Fig. 3. This is because a smaller value of  $\kappa$  leads to a drastic reduction of the emission. As a consequence of this suppressed emission, the temperature remains close to its initial value,  $T_0$ , for a long period of time,  $t \sim 10^3$  seconds. [1] selected observations such that XMM-Newton would always point away from the Earth and Sun. Therefore, we expect that their signal will be weakly sensitive to  $T_0$  and strongly sensitive to  $\kappa$ .

We conclude this section with a few comments on the parameters  $T_0$  and  $\kappa$ , which appear in the computations and provide a benchmark for our numerical estimates. As we shall see in the next section, the spectrum and the intensity of the emission depend on these parameters in a very nontrivial way. As already mentioned at the beginning of this section, the exit temperature is expected to be in the range  $T_0 \sim 200 \text{ keV}$  according to (6). The other parameter which enters our computations is the suppression factor,  $\kappa$ , defined by Eq. (7). This was introduced to account for the drastic decrease of the positron number density from the electrosphere, which can emit photons. This strong suppression is a direct consequence of high internal temperature,  $T_0$ , when a large number of weakly bound positrons are expanded over much larger distances order of  $R$  rather than distributed over much shorter distances of order  $\bar{z}$  defined by eq.(4). The

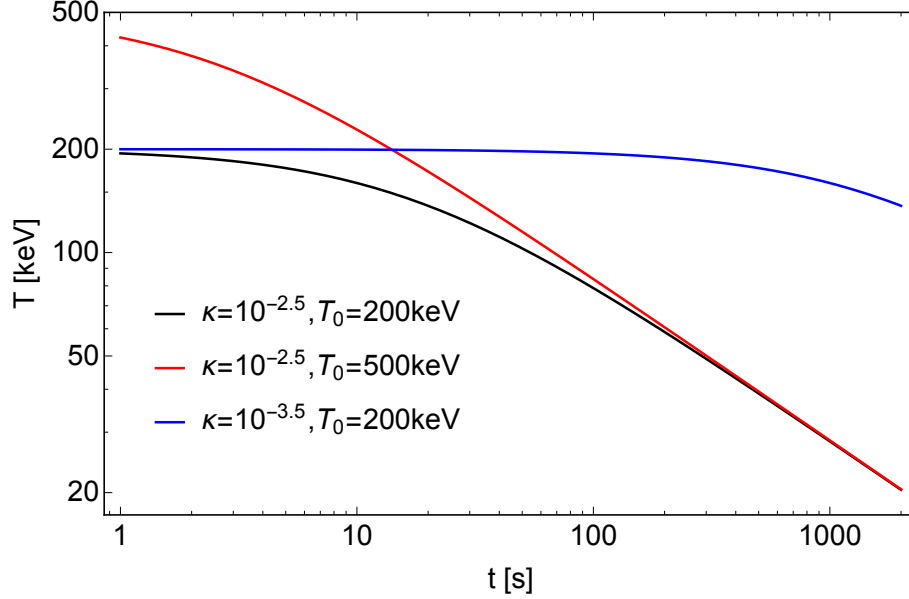


Figure 3:  $T$  vs.  $t$  for different values of  $\kappa$  and  $T_0$ .  $T = T_0$  at  $t = 0$ . An important feature here is that the behaviour  $T(t)$  at  $t \geq 100$  s (when XMM-Newton becomes operational) is not sensitive to the initial value of  $T_0$ , see text for explanations.

corresponding estimates had been carried out in Appendix A in [29] which explicitly shows the emergence of very small factor  $(mR)^{-1/2}$  as a manifestation of this effect, i.e.

$$\kappa \sim \left(\frac{\bar{z}}{R}\right)^{\frac{1}{2}} \sim \frac{1}{\sqrt{mR}} \frac{1}{\sqrt[4]{2\pi\alpha}} \sim 2 \cdot 10^{-3}. \quad (19)$$

Again, we opted to treat  $\kappa$  as a free phenomenological parameter in the rest of the paper, similar to the parameter  $T_0$  discussed above. The benchmark value for  $\kappa$  is given by (19).

#### 4. Computation of the spectrum and Comparison with XMM-Newton data

This is the central section of the present work, as we are in a position to compute the spectrum and intensity received by XMM-Newton from the thermal emission of nuggets computed in the previous section.

We start with the simplified assumption that the nuggets are *uniformly* distributed around the Earth. We will also assume that the nuggets exit the Earth *radially*. As we shall see below, we are able to reproduce the spectrum observed by XMM-Newton with the AQN framework. Since the calculations are relatively insensitive to the free parameters of the model, our result represents a very generic consequence of the system when the spectrum is essentially determined by the “soft photon theorem,” as we already mentioned at the end of subsection 3.1.

In what follows, we compute the spectrum and the intensity with the assumptions formulated above. The corresponding result on the spectrum is not very sensitive to the specific geometry since the X-ray emission from the nugget is isotropic and does not depend on the direction of velocity, nor the orientation with respect to Earth. At the same time, the intensity is highly sensitive to the parameters as we discuss below. With these simplifications in mind, the number density of nuggets that have passed through the Earth is

$$n_{\text{AQN}}(s) = \frac{1}{4\pi(R_{\oplus} + s)^2} \cdot \frac{\mathcal{F}}{v_{\text{out}}}, \quad (20)$$

where Fig. 4 shows the geometry of the configuration. In Eq. (20),  $s$  denotes the distance from the Earth's surface.  $v_{\text{out}}$  is the nugget's velocity leaving the Earth's surface, which is assumed to be the same for all nuggets and independent of  $s$ . For simplicity, we approximate  $v_{\text{out}} \simeq v_{\text{in}}$ , the nugget's velocity when it hits the Earth, although the nuggets may be slowed down by the interactions with their surroundings inside the Earth. This approximation is good enough for our analytical treatment in this section. The effect of the velocity difference between  $v_{\text{out}}$  and  $v_{\text{in}}$  will be discussed in the next section where this difference plays a key role in our studies of the seasonal variations. We should also note that  $n_{\text{AQN}}$  is a season invariant, see Appendix C with details. We denote  $\mathcal{F}$  as the total nugget flux (number per unit time) that hits the Earth. It has been estimated as follows [18]:

$$\mathcal{F} \simeq 0.67 \text{ s}^{-1} \left( \frac{\rho_{\text{DM}}}{0.3 \text{ GeV/cm}^3} \right) \left( \frac{v_{\text{in}}}{220 \text{ km/s}} \right) \left( \frac{10^{25}}{\langle B \rangle} \right). \quad (21)$$

We adopt the following values for our numerical estimates:  $v_{\text{out}} \simeq v_{\text{in}} \simeq 220 \text{ km/s}$ ; average baryon charge,  $\langle B \rangle = 10^{25}$  (which corresponds to an average size of the nugget,  $\langle R \rangle = 2.25 \cdot 10^{-5} \text{ cm}$ ). This corresponds to a total flux of  $\mathcal{F} \simeq 0.67 \text{ s}^{-1}$  [18].

Fig. 4 shows the positions of the Earth and the XMM-Newton observatory. It also shows how the XMM-Newton observatory receives the radiation from a large number of nuggets, with number density  $n_{\text{AQN}}$ , surrounding the Earth. Various configuration parameters are defined in Fig. 4's caption. The following geometric relations are useful:

$$\begin{aligned} s_{\text{mid}}(\theta) &= \frac{L'}{-\cos\theta} - R_{\oplus}, \quad y_{\text{mid}}(\theta) = -L' \tan\theta, \\ r_{\text{mid}}(\theta) &= (y_{\text{mid}} + L) \tan\alpha_c. \end{aligned} \quad (22)$$

The number of nuggets inside the thin disk of the cone (shown in Fig. 4) is

$$dN(\theta) = n_{\text{AQN}} dV = n_{\text{AQN}} [s_{\text{mid}}(\theta)] \cdot \pi r_{\text{mid}}^2(\theta) dy_{\text{mid}}(\theta). \quad (23)$$

The distance,  $s_{\text{mid}}$ , and the time,  $t$ , are connected by the nugget velocity,  $v_{\text{out}}$ :  $s_{\text{mid}} = v_{\text{out}} t$ . The spectrum received by the XMM-Newton observatory can be calculated as:

$$\begin{aligned} \frac{dF_r}{d\omega} &= \int_{\text{cone}} \frac{dF}{d\omega}(T_{\text{mid}}, \omega) \frac{R^2}{[y_m(\theta) + L]^2} dN(\theta) \\ &= \int_{\frac{\pi}{2}}^{\pi + \arctan(L/L')} d\theta \left\{ \frac{dF}{d\omega}(T_{\text{mid}}, \omega) \frac{R^2}{[y_m(\theta) + L]^2} \right. \\ &\quad \left. \cdot n_{\text{AQN}} [s_{\text{mid}}(\theta)] \cdot \pi r_{\text{mid}}^2(\theta) \frac{L'}{\cos^2\theta} \right\}, \end{aligned} \quad (24)$$

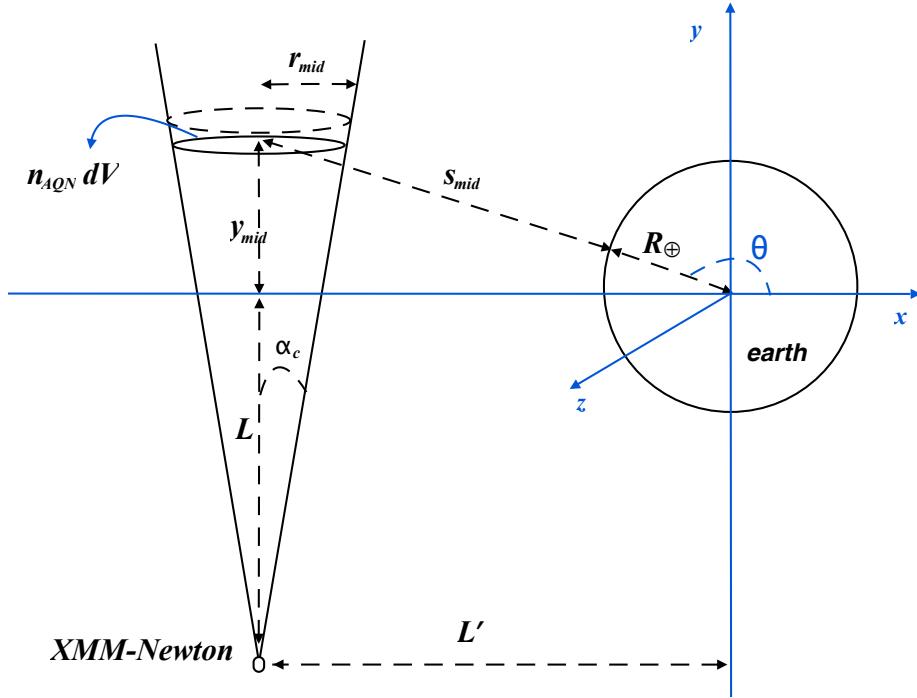


Figure 4: The XMM-Newton observatory is assumed to be located at the position  $(x, y, z) = (-L', -L, 0)$ . The cone is the field of view of the EPIC pn camera carried by XMM-Newton. In our present work, we focus on this camera (see footnote 6 for details). The cone points in the direction  $+y$ .  $dV$  is the volume of the thin disk, and the number of nuggets contained inside is  $n_{\text{AQN}} dV$ .  $r_{\text{mid}}$  is the radius of the thin disk. Since the opening angle of the cone is very small,  $\alpha_c = 0.25$  deg, it is a good approximation that all nuggets inside  $dV$  are located at the same point  $(-L', y_{\text{mid}}, 0)$ .  $y_{\text{mid}}$  could be negative, so they have the same distance,  $s_{\text{mid}}$ , to the Earth's surface. The range of  $\theta$  is apparently  $[\pi/2, \pi + \arctan(L/L')]$ .

where  $\frac{dF}{d\omega}(T_{\text{mid}}, \omega)$  is the spectral surface emissivity computed at the moment  $t_{\text{mid}} = \left[ \frac{s_{\text{mid}}(\theta)}{v_{\text{out}}} \right]$  with the corresponding temperature,  $T_{\text{mid}}$ . The computations of  $\frac{dF}{d\omega}(T, \omega)$  for arbitrary  $T$  have been carried out in section 3.1, see Fig. 2 for example. The  $R$  in Eq. (24) is the nugget's radius,  $R \simeq 2.25 \cdot 10^{-5} \text{cm}$ , corresponding to  $\langle B \rangle = 10^{25}$ . For numerical estimates, we consider two different options (please refer to Fig. 4 for the geometry): first we consider the observatory locating at position A:  $(x, y, z) = (-7, -7, 0)R_{\oplus}$ , where  $R_{\oplus}$  is the Earth's radius. Secondly we consider the observatory locating at position B:  $(x, y, z) = (-8, -6, 0)R_{\oplus}$  with the cone orientation keeping unchanged, for the same three groups of  $(\kappa, T_0)$ . We observe very minor changes as a result of this modification of the geometry<sup>4</sup>, see Fig. 5. These modifications are much smaller than changes due to variation of parameters  $T_0$  and  $\kappa$  which cannot be computed precisely, as explained in the previous section. Therefore, later when we make the contour plot (Fig. 6) to explore the parameter space of  $\kappa$  and  $T_0$  and when we discuss the seasonal variation, we consider only single option A as any small modifications of location lead to very minor variations for the intensity. One should emphasize that the spectrum of the emission is not sensitive to any changes of the parameters as we explain below.

The radiation spectrum  $dF_r/d\omega$  given by (24) is the energy received by the observatory per unit time, per unit area, and per unit frequency. In order to make a precise comparison between our calculations and the observations [1], we convert  $dF_r/d\omega$  to  $f^{(\text{theory})}$ , the *number of photons* received by the observatory per unit time, per unit area, per unit frequency, and *per unit solid angle*, which is defined as follows:

$$f^{(\text{theory})} \equiv \frac{1}{\Omega_c} \frac{1}{\omega} \frac{dF_r}{d\omega}, \quad (25)$$

where  $\Omega_c = 2\pi(1 - \cos \alpha_c) \approx 5.98 \times 10^{-5} \text{sr} \approx 0.196 \text{deg}^2$  is the solid angle of the cone. The corresponding theoretical prediction is plotted in Fig. 5, for several typical values of the parameters of the system,  $\kappa, T_0$ , as discussed in Section 3.

In order to compare with observations from XMM-Newton in the 2-6 keV energy band, we use the power-law fit, as given by [1], see Eq. (11) from that paper<sup>5</sup>:

$$f^{(\text{obs})} = N_0 \left( \frac{\omega}{\text{keV}} \right)^{-\Gamma} \frac{1}{\text{cm}^2 \cdot \text{s} \cdot \text{keV} \cdot \text{sr}}. \quad (26)$$

The normalization factor  $N_0$  is dimensionless, while  $f$  is measured in  $[\text{cm}^{-2} \text{s}^{-1} \text{keV}^{-1} \text{sr}^{-1}]$ . For the EPIC pn camera carried by XMM-Newton<sup>6</sup>, the values of the numerical pa-

<sup>4</sup>The orbit of XMM-Newton is highly elliptical, with an apogee altitude of  $\sim 115000 \text{km}$  and a perigee altitude of  $\sim 6000 \text{km}$ . The orbit period is  $\sim 48 \text{hr}$ . The orbit changes with time, due to several perturbations. We refer the readers to the XMM-Newton Users Handbook [32] for details. The observatory only works at altitudes above the Earth's radiation belts  $\sim 46000 \text{km}$ , see, e.g., [32, 33]. Therefore, in this section, we choose  $L = 7R_{\oplus}$ , which implies that the altitude of the observatory is  $\sqrt{2}L - R_{\oplus} \approx 57000 \text{km}$ .

<sup>5</sup>The symbols in Eq.(11) of [1] conflict with ours, so we rewrite Eq. (11) as (26), using our own symbols to avoid confusion.

<sup>6</sup>XMM-Newton carries three cameras that are relevant to us: EPIC pn, EPIC MOS1, and EPIC MOS2.



parameters  $(N_0, \Gamma)$  are:

$$\begin{aligned}
\text{Winter}(N_0, \Gamma) &= (6.66, 0.97); \\
\text{Spring}(N_0, \Gamma) &= (9.08, 0.98); \\
\text{Summer}(N_0, \Gamma) &= (9.60, 1.06); \\
\text{Fall}(N_0, \Gamma) &= (12.09, 0.97),
\end{aligned}
\tag{27}$$

see Table 3 in [1]. These numbers are obtained by fitting the data observed by the EPIC pn camera (from Fig. 1) showing the seasonal variation of the X-ray background with  $11\sigma$  significance. The maximum amplitude of the seasonal variation from these data occurs between Winter and Fall, rather than between Winter and Summer. It has been discussed in [1] and will be discussed in the context of the AQN model in section 5.2.

Fig. 5 shows our theoretical prediction (the solid lines and dotted lines from Eq. (25)) against the observed spectra (the dashed lines from Eq. (26)) for four seasons. The similarity between the observations and theoretical computations is impressive, considering that the shape of the predicted radiation spectrum is only slightly sensitive to the parameters  $\kappa$  and  $T_0$ . This result is a direct consequence of the AQN framework<sup>7</sup>. The basic reason for the robustness of our prediction is that the spectrum shape is essentially determined by the very fundamental “soft photon theorem,” with a specific behaviour,  $d\omega/\omega$ , for  $\omega \ll T$ , as we already emphasized earlier at the end of subsection 3.1. The slope,  $\Gamma$ , as seen in Eq. (26), is indeed very close to  $\Gamma \simeq 1$  for all seasons. This shows very strong support for our AQN framework, as the spectrum is very robust consequence of the framework, not sensitive to specific details of the computations.

The intensity of the emission, on the other hand, is sensitive to the parameters  $(\kappa, T_0)$ . It is also sensitive to the dark matter distribution, nugget size distribution, velocity distribution, etc., as one can see from Eq. (21) for the AQN flux. The distance and orientation of the *XMM-Newton* will also play a role in the seasonal variation. Some of these effects will be discussed in Section 5.

We can use our analytical predictions to explore the  $(\kappa, T_0)$  parameter range that is consistent with the observations shown in Fig. 1. For this purpose, we calculate the maximum likelihood  $\mathcal{L}(\kappa, T_0)$  defined as:

$$\mathcal{L}(\kappa, T_0) = \exp \left[ -\frac{1}{2} \left( \frac{d - f(\kappa, T_0)}{\sigma} \right)^2 \right],
\tag{28}$$

where the data,  $d$ , and the model,  $f(\kappa, T_0)$ , are estimated at one particular frequency,  $\omega$ . We choose  $\omega = 3$  keV, but any frequency would work, since the model and the

---

The three cameras all clearly show the seasonal variance of the X-ray background with similar values of  $(N_0, \Gamma)$  listed in the main text, which can be seen in Table 3 of [1]. Therefore, we only need to focus on one camera, which is enough for our purpose in the present work to compare the AQN-based calculations with the observations. We choose the EPIC pn camera because it has the largest photon grasp (effective area  $\times$  aperture), which is a key parameter in studying the background of X-ray radiation, and because it has better counting statistics than the two EPIC MOS cameras [1].

<sup>7</sup>A cusp behavior in the region  $\omega = 1-2$  keV in Fig. 5 has no physical significance. Rather, it is a reflection of our simplified treatment of the regions with small  $\omega$ , which results in such a cusp singularity, see comments on this cusp behaviour in subsection 3.1.

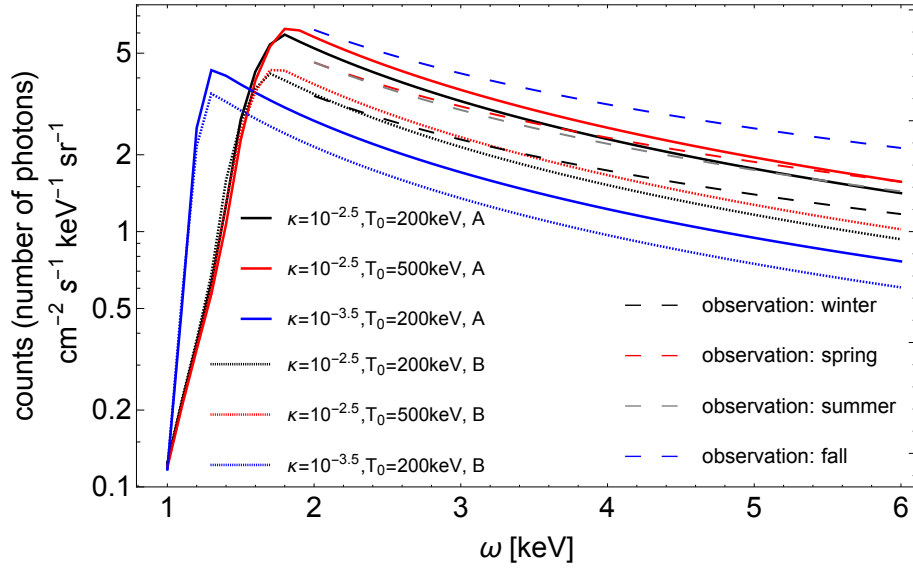


Figure 5: The relation  $f$  vs.  $\omega$ , (25), for  $(\kappa, T_0) = (10^{-2.5}, 200 \text{ keV})$ ,  $(10^{-2.5}, 500 \text{ keV})$ , and  $(10^{-3.5}, 200 \text{ keV})$  respectively. The x-axis represents frequency. The y-axis represents the values of  $f^{(\text{theory})}$ , given by (25), which is the number of photons received by the XMM-Newton observatory (camera EPIC pn) per unit time, per unit area, per unit frequency, and per unit solid angle in the AQN framework. The solid lines are for the case that the XMM-Newton observatory locates at position A:  $(x, y, z) = (-7, -7, 0)R_{\oplus}$ . In comparison, we also plotted the spectra for the second option that the observatory locates at position B:  $(x, y, z) = (-8, -6, 0)R_{\oplus}$  with the cone orientation keeping unchanged, for the same three groups of  $(\kappa, T_0)$ , which are denoted as dotted lines. We also plot  $f^{(\text{obs})}$ , given by (26), representing the data observed by the EPIC pn camera for four seasons, shown by the four dashed lines respectively.

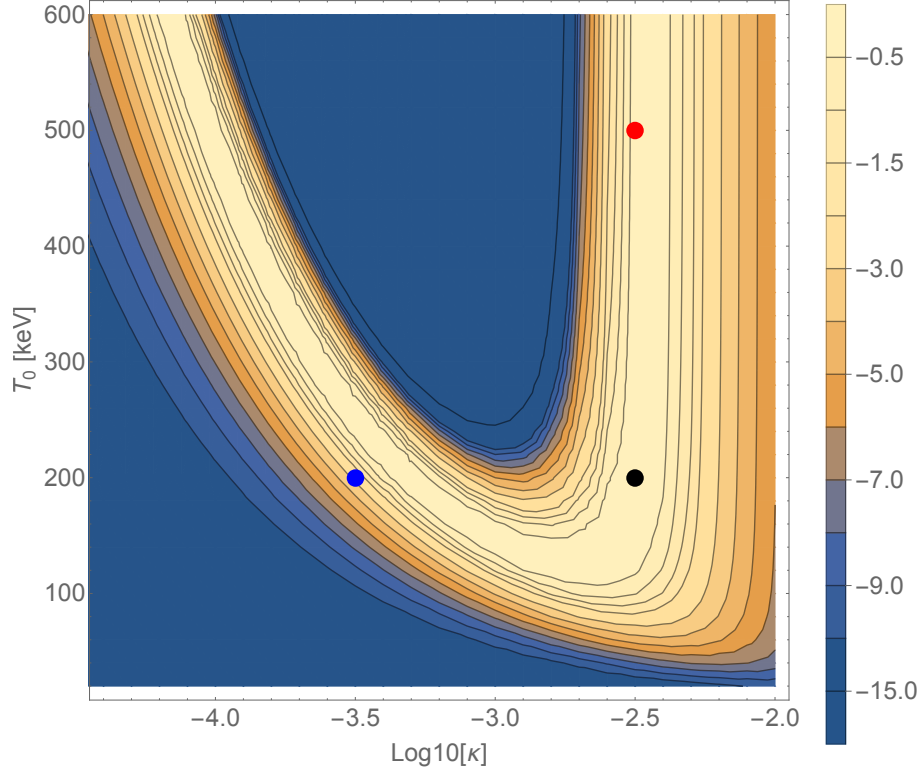


Figure 6: The contour plot of  $2 \ln \mathcal{L}(\kappa, T_0)$ . The numbers on the color bar represent the values of  $2 \ln \mathcal{L}$ . The three points marked on the plot are the three sets of  $(\kappa, T_0)$  that we have chosen in all of our previous plots:  $(10^{-2.5}, 200 \text{ keV})$ ,  $(10^{-2.5}, 500 \text{ keV})$ , and  $(10^{-3.5}, 200 \text{ keV})$ .

observations show a very similar frequency dependence. The value of  $d$  in Eq. (28) is chosen as the middle of the four observed spectra, which is defined as the average of the top spectrum (Fall) and bottom spectrum (Winter), i.e.  $d \equiv \frac{1}{2}[f^{(\text{obs},\text{F})} + f^{(\text{obs},\text{W})}]$ . The variance,  $\sigma$ , is chosen as  $\sigma \equiv \frac{1}{2}[f^{(\text{obs},\text{F})} - f^{(\text{obs},\text{W})}]$ , which represents the maximum signal variation between the four seasons. Note that we are not in a position to calculate a full likelihood function over all frequencies, since we do not know the correlation for different  $\omega$ , and the resulting likelihood would be difficult to interpret. Nevertheless, our approach should provide a reasonable order of magnitude estimate of the region of the parameter space,  $(\kappa, T_0)$ , consistent with the observations. We are not trying to interpret  $\mathcal{L}(\kappa, T_0)$  in a probabilistic way because our error estimate is only approximate. However, the maximum of  $\mathcal{L}(\kappa, T_0)$  at 1 is still a valid indicator of where the  $(\kappa, T_0)$  degeneracies lie. Fig. 6 shows the iso-contours of  $2 \ln \mathcal{L}(\kappa, T_0)$ , where a lighter colour represents a better match. The allowed parameter space is represented by two branches in Fig. 6. The right vertical branch is essentially independent of  $T_0$ , and it matches the observations for  $\kappa \sim 10^{-2.5}$ . This “insensitivity” to  $T_0$  is consistent

with the red and black lines in Fig. 3, which illustrates the fact that AQN cooling is independent of  $T_0$  when  $\kappa$  is high enough. On the other hand, the left branch is strongly dependent on both  $\kappa$  and  $T_0$ . The next step is to investigate the seasonal variation in the context of our model. From the qualitative arguments given in Section 3.2, the physically preferred values for  $\kappa$  and  $T_0$  are in the right branch. However, for completeness, we will also calculate the seasonal variations for a lower value of  $\kappa$ . In the next section, the calculations will be restricted to the three sets of parameter values represented by the big solid dots in Fig. 6.

We conclude this section with the following comment. Our computation of the spectrum (including the extension to much higher energies) is robust and can be used to plan future experiments to perform the annual modulation studies in the near-Earth environment without any modulation due to the seasonal variations. In the next Section we discuss the impact of the Earth position (subsection 5.1) and the possible complications due to the telescope altitude and orientation (subsection 5.2).

## 5. Seasonal variation

Up to this section, our focus was on the calculation of the average intensity of the AQN radiation spectrum, ignoring the seasonal variations. However, the seasonal variation was the most important feature discovered by [1] as the conventional paradigm assumes that there should be no any seasonal variations as mentioned in Introduction. The authors claimed an  $11\sigma$  confidence level detection of the seasonal variation in the 2-6 keV energy band, after removing all possible instrumental contamination and known astrophysical sources. They argued that known conventional astrophysical sources had been ruled out as a possible explanation of their signal. The main goal of this section is to explain how the seasonal variation might occur in the AQN framework. We will find that an annual amplitude modulation on the order of 20-25% is expected. Interestingly, with conventional dark matter models (e.g. WIMPs), any seasonal variation is expected at a much lower level, on the order of 1-10% for most of the experiments carried out on Earth's surface when the effect is entirely due to the flux differences, see, e.g., [19] and [20].

### 5.1. Effect of the Earth's position on its orbit

In Section 4, we introduced  $v_{in}$ , the speed of a nugget hitting the Earth. However, the Earth's motion around the Sun leads to a seasonal variation of  $v_{in}$ , which will affect the AQN signal given by Eq. (24). In this subsection, we will calculate the amplitude of the seasonal effect, using the analytical prediction, Eq. (24), and a realistic model of a nugget's incoming speed,  $v_{in}$ , which is different in the Winter and Summer.

The Sun is moving in the galactic plane, on a nearly circular orbit with velocity,  $v_{DMG}$ , about the galactic center. The rotation of the dark matter halo is negligible compared to the rotation of the Sun. Therefore, the entire solar system is facing a dark matter wind with an average velocity of approximately  $v_{DMG}$ . The tilt of the ecliptic plane relative to the dark matter wind is approximately  $60^\circ$ . This configuration is shown in Figure 7, along with the positions of the four seasons on the Earth's orbit.

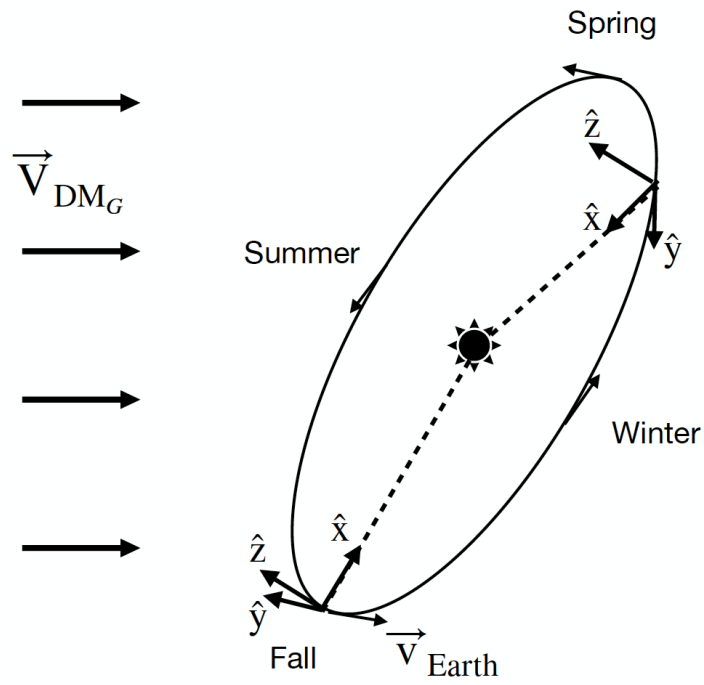


Figure 7: Motion of dark matter relative to the Solar System, which is taken as the fixed reference frame. The Earth moves in a nearly circular orbit, with a velocity,  $\vec{v}_E$ , relative to the Sun. The location of the seasons relative to the orientation of the ecliptic plane and dark matter wind,  $v_{DM_G}$ , is important for the effect discussed in Section 5.

The dark matter velocity with respect to the Sun is  $\vec{v}_{\text{DM}_G}$ , with  $v_{\text{DM}_G} \simeq 220$  km/s. The velocity of the Earth around the Sun is  $\vec{v}_E$ , with  $v_E = 30$  km/s. Consequently, the dark matter velocity with respect to the Earth is given by

$$\vec{v}_{\text{in}} = \vec{v}_{\text{DM}_G} - \vec{v}_E, \quad (29)$$

and the magnitude is

$$v_{\text{in}} = \sqrt{v_{\text{DM}_G}^2 + v_E^2 - 2v_{\text{DM}_G} \cdot v_E \cdot \cos \theta}, \quad (30)$$

where  $\theta$  is the angle between  $\vec{v}_E$  and  $\vec{v}_{\text{DM}_G}$ .  $\theta$  is  $60^\circ$  in the Winter,  $120^\circ$  in the Summer, and  $90^\circ$  in the Spring and Fall. Noting that  $v_{\text{DM}_G} \gg v_E$ , (30) can be simplified via Taylor expansion as

$$v_{\text{in}} \simeq v_{\text{DM}_G} - v_E \cos \theta. \quad (31)$$

Using this approximation, the magnitude of the dark matter velocities (with respect to the Earth) in the four seasons is given by:

$$\begin{aligned} v_{\text{in}}^{(\text{Sp})} &= v_{\text{in}}^{(\text{F})} \simeq v_{\text{DM}_G}, \\ v_{\text{in}}^{(\text{W})} &\simeq v_{\text{DM}_G} - \Delta v, \\ v_{\text{in}}^{(\text{S})} &\simeq v_{\text{DM}_G} + \Delta v, \end{aligned} \quad (32)$$

where  $\Delta v = \cos(60^\circ) \cdot v_E = 15$  km/s.  $\Delta v$  is the deviation from 220 km/s, caused by the Earth's revolution around the Sun. The result is that the dark matter velocity is different for different seasons, as is apparent in Eq. (32), which leads to the seasonal variation of the X-ray background.

There are two specific features which are not shared by conventional WIMP models. The first one is related to the fact that the  $v_{\text{in}}$  and  $v_{\text{out}}$  velocities are different in the AQN model, but not in conventional dark matter. The second one is related to the fact that the intensity of the radiation explicitly depends on the number of nuggets which can be seen by the detector at each given moment, as shown in Fig. 4 and computed in Eq. (24). As we will see below, this leads to a feature unique to the AQN framework that is not shared by conventional dark matter.

The first effect, related to  $v_{\text{out}} \neq v_{\text{in}}$ , can be explained as follows. The passage of the AQN through the Earth is accompanied by friction and annihilation events with the surroundings, leading to  $v_{\text{out}} < v_{\text{in}}$ . We used  $v_{\text{out}} = v_{\text{in}} = 220$  km/s in Section 4, a simplification that was sufficient to estimate the average of the AQN-induced spectrum. However, in this section, the fact that  $v_{\text{out}}$  is smaller than  $v_{\text{in}}$  may have an important impact on the seasonal variation. The reason is that as  $v_{\text{out}}$  gets closer to  $\Delta v$ , the seasonal variation becomes relatively more important. Different nuggets have different paths through the Earth, which results in different  $v_{\text{out}}$  even for the same  $v_{\text{in}}$ . The precise distribution of  $v_{\text{out}}$  can only be obtained by numerical simulations, which is well beyond of the scope of the present work. The speed change from crossing the Earth is quantified by the parameter  $\gamma$ :

$$\gamma = \frac{v_{\text{out}}}{v_{\text{in}}}, \quad (33)$$

which is assumed to be constant in the present work, but may vary for different trajectories and different nugget's sizes. Combining Eq. (32) with Eq. (33), we obtain the following expressions for  $v_{\text{out}}$  in the four seasons:

$$\begin{aligned} v_{\text{out}}^{(\text{Sp})} &= v_{\text{out}}^{(\text{F})} \simeq \gamma v_{\text{DMG}}, \\ v_{\text{out}}^{(\text{W})} &\simeq \gamma(v_{\text{DMG}} - \Delta v), \\ v_{\text{out}}^{(\text{S})} &\simeq \gamma(v_{\text{DMG}} + \Delta v). \end{aligned} \quad (34)$$

The second effect is due to the fact that the number of nuggets passing through the detection cone of the XMM-Newton detector depends on  $v_{\text{out}}$  as well, as shown in Fig. 4. Using Eq. (24), the *average*  $dF_r/d\omega$  measured by the detector is given by:

$$\frac{dF_r}{d\omega} \simeq n_{\text{AQN}}(\bar{s})V \cdot \frac{dF}{d\omega}[T(\bar{s})], \quad (35)$$

where  $\bar{s}$  denotes the *average* distance of the nuggets inside the cone, as viewed from the Earth's surface. The quantity  $n_{\text{AQN}}(\bar{s})$  is the number density of nuggets at distance,  $\bar{s}$ , while  $\frac{dF}{d\omega}[T(\bar{s})]$  is the spectrum emitted by a single nugget at distance,  $\bar{s}$ , determined by the temperature,  $T(\bar{s})$ . The volume,  $V$ , is the effective volume of the cone, which is a constant, inside which the nuggets contribute to the total spectrum received by XMM-Newton. This means that we do not consider nuggets that are too far away from the detector. The detailed calculation of Eq. (35) is shown in Appendix Appendix C, where we obtain an expression of  $dF_r/d\omega$  as a function of  $v_{\text{out}}$ :

$$\frac{dF_r}{d\omega} \propto \left( \frac{K_1}{v_{\text{out}}} + K_2 \right)^{-\frac{3.22}{c_2(\kappa)+3}}, \quad (36)$$

where  $K_1$  and  $K_2$  are functions of  $\kappa$  and  $T_0$  (see Appendix Appendix C for details).

The maximum seasonal difference is expected between Summer and Winter, because they have the maximum velocity difference,  $2\gamma\Delta v$ , as seen from Eq. (34). We define the ratio

$$r \equiv \frac{\left( \frac{dF_r}{d\omega}^{(\text{S})} \right)}{\left( \frac{dF_r}{d\omega}^{(\text{W})} \right)} \quad (37)$$

as the difference between the Summer and Winter spectra. Using Eq. (34) and Eq. (36), we get

$$r \simeq \left[ \frac{\gamma^{-1}K_1/(v_{\text{DMG}} + \Delta v) + K_2}{\gamma^{-1}K_1/(v_{\text{DMG}} - \Delta v) + K_2} \right]^{-\frac{3.22}{c_2(\kappa)+3}}, \quad (38)$$

where  $v_{\text{DMG}} = 220$  km/s and  $\Delta v = 15$  km/s, as discussed above.

The functions  $K_1$  and  $K_2$  play a very important role in our study. If the temperature,  $T$ , strongly deviates from its initial value,  $T_0$ , such that  $T \ll T_0$  at the moment of observation, then the second term with  $T_0$  in the brackets in Eq. (B.1) can be ignored, which drastically simplifies all equations. In particular, the term  $K_2 \sim T_0^{-[c_2(\kappa)+3]}$  in Eq. (C.6) can be neglected. This implies that  $K_2$  in Eq. (36) can be also ignored, which drastically simplifies the analysis.

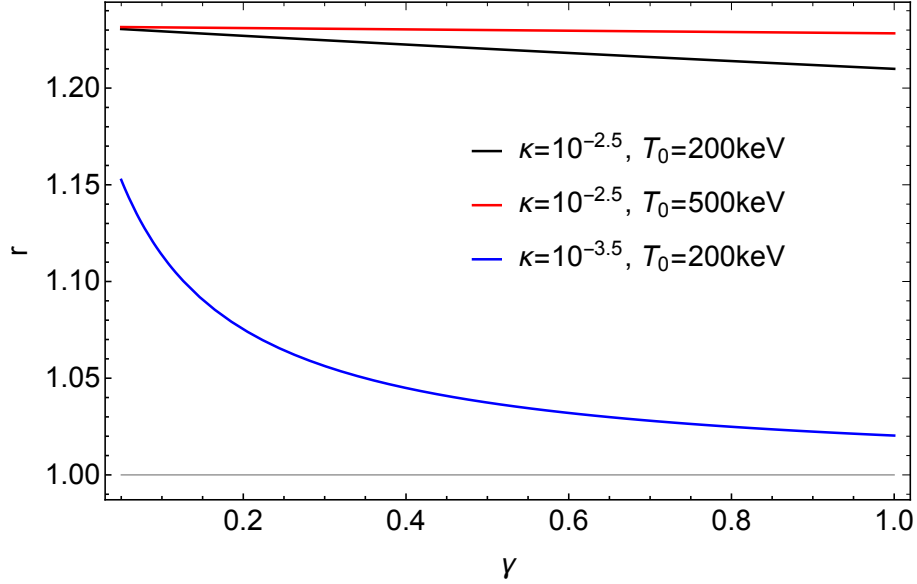


Figure 8: The ratio  $r$  as a function of  $\gamma$  for different groups of  $\kappa$  and  $T_0$ . The solutions from the right branch from Fig. 6 (red and black lines) will always produce  $r \approx 20\%$  irrespectively to the value of  $\gamma$ , while the solution from left branch from Fig. 6 (blue line) will always generate a very small value of  $r$ .

In this case, Eq. (38) can be simplified to

$$r \simeq \left( \frac{v_{\text{DMG}} + \Delta v}{v_{\text{DMG}} - \Delta v} \right)^{\frac{3.22}{c_2(\kappa)+3}} \approx 1.23, \quad (39)$$

which does not depend on  $\gamma$ . This is a very solid and robust consequence of the AQN model. One should also emphasize that the condition  $T \ll T_0$  is always satisfied for all solutions on the right branch shown in Fig 6. Indeed, the temperature,  $T$ , drastically drops for any value of  $T_0$  with  $\kappa \simeq 10^{-2.5}$ , as shown in Fig. 3.

Eq. (39) is a very important result. It shows that for solutions from the right branch of Fig. 6, the seasonal variation could be large, up to  $\sim 20\text{-}25\%$ , relatively insensitive to the exact value of  $\gamma$ . Fig. 8 shows the results of the exact computation from Eq. (38) supporting this claim, where the red and black lines remain relatively flat at  $r \approx 1.23$  for all values of  $\gamma$ . The solutions from the left branch lead to a considerably smaller amplitude of the seasonal variation for any values of  $\gamma$ , as illustrated by the blue line in Fig. 8. In the context of the AQN framework, the result (39) provides a strong argument in favour of a solution in the right branch of Fig. 6, because only the right one is capable of leading to seasonal variations in agreement with [1].

As an example of seasonal variation, Fig. 9 shows  $f^{(\text{theory})}$ , as defined by Eq. (25), with  $\frac{dF_r}{d\omega}$  given by Eq. (24). For this plot, we choose  $\kappa = 10^{-2.5}$ ,  $T_0 = 200$  keV, and  $\gamma = 1/2$ . However, as we have shown in the previous sections, the radiation spectrum is not very sensitive to parameters  $T_0$  and  $\gamma$ , as long as we choose a solution from the right branch of Fig. 6. A sample of the spectrum with  $\omega \in 2\text{-}3$  keV shows a large



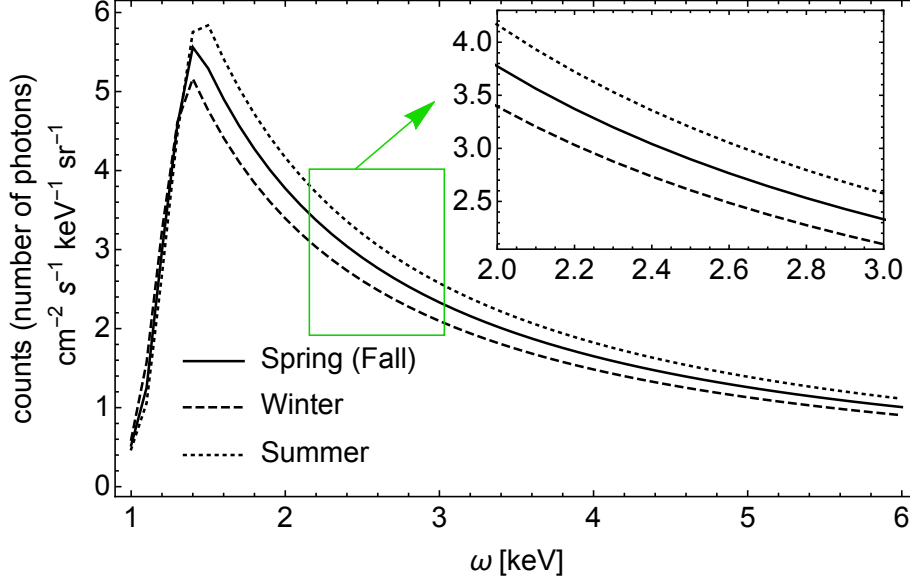


Figure 9: Demonstration of the seasonal variation with specific parameters  $(\kappa, T_0, \gamma) = (10^{-2.5}, 200 \text{ keV}, 0.5)$  as an example. A small portion of the spectrum,  $\omega \in 2\text{-}3 \text{ keV}$ , is zoomed in to demonstrate a large seasonal variation on the level of  $\approx 20\%$ .

seasonal variation at the level of  $\sim 20\text{-}25\%$ .

The maximal seasonal variation observed by [1] can be estimated from normalization factors,  $N_0$ , given by Eq. (27) for different seasons as follows:

$$\frac{N_0(\text{Fall}) - N_0(\text{Winter})}{N_0(\text{Fall}) + N_0(\text{Winter})} \approx 0.29, \quad (40)$$

which is a very large effect. One should emphasize that the seasonal variation (40) cannot be directly compared with our estimate of parameter  $r$ , computed for Summer-Winter modulation (39). This is due to the satellite's positions and the orientations of the detector, which will be discussed in Subsection 5.2. The main lesson of our computations is that the annual modulation effect is very large, much larger than conventional WIMP models can predict [19, 20], which are on the level of 1-10% computed at the Earth's surface.

### 5.2. Effect of the satellite's position and orientation on its orbit

The previous calculations show that we should expect a seasonal modulation of the signal, which should be strongest in Summer, weakest in Winter, and equally half-way for Fall and Spring. This effect is entirely driven by the strength of the local dark matter wind speed. Compared to Fig. 1, one can see that this does not quite agree with the seasonal modulation measured by [1], as given by (27). In their measurement, the Fall amplitude is the highest, and Summer and Spring are equal. However, as noted by [1], there are two additional factors which can change the seasonal modulation of the X-ray

background significantly: the altitude of the telescope and the direction of the field-of-view (or beam). These factors are particularly important in the context of our model. Firstly, the altitude plays a role because, as shown by Eq. (35), a nugget's temperature upon exiting Earth decreases quickly with altitude. Therefore, if the telescope observes from a high altitude out, the X-ray background should be lower than if observed from a lower altitude. Secondly, the orientation of the telescope beam is also important. The X-ray background will indeed be stronger in the direction opposite to the incoming dark matter wind. This is caused by the fact that, on average, more heated nuggets will emerge from the side of the Earth opposite to the side where they preferentially entered from. Consequently, depending on the telescope position and orientation, the seasonal variation of the X-ray background can be altered.

The reason that these effects could be potentially very strong is because the XMM-Newton is placed on a Highly-elliptical Earth Orbit (HEO), with an inclination of  $40^\circ$  relative to the ecliptic plane, a southern apogee altitude of  $\sim 115000$  km, and a perigee of  $\sim 6000$  km, with an orbital period of 48 hours. The exact prediction of the X-ray background becomes a highly non-trivial task, which requires precise knowledge of the telescope position and orientation for every data point being taken, which is beyond the scope of the present work.

## 6. Conclusion

The observation [1] of the seasonal variations in the Cosmic X-ray Background residual is a highly unexpected phenomenon. We propose an explanation which avoids the issues of the model based on solar axions proposed by [1]. Our suggestion is that dark matter is made of AQNs which occasionally cross the Earth, and when they emerge they emit X-rays that contribute to the near-Earth X-ray background. The main results of the present work can be summarized as follows:

1. Our estimations for the expected signal are presented in Fig.9. In the 2-6 keV energy band, it is consistent with the intensity and spectral shape observed by [1];
2. We computed the spectrum and the intensity of the AQNs emission where XMM-Newton is operational, i.e.  $r \gtrsim 8R_\oplus$ . The corresponding results are presented in Fig. 5 and shown by the solid lines;
3. The obtained results are consistent with the energy spectrum observed by [1], which are also shown in Fig. 5 with the four dashed lines (for the four seasons). The important point is that the shape of the spectrum is not sensitive to any details of the model, and represents very solid and robust predictions of the entire AQN framework. We did not attempt to reproduce the seasonal variation shown on Fig. 1) which requires the precise position and orientation of the telescope and is left for future work. This was explained in subsection 5.2;
4. This spectrum extends to much higher energies, up to 100 keV. This should be considered as a very robust prediction of the AQN framework. It can be tested in future experiments by any instrument sensitive to energies above 6 keV, representing

the XMM-Newton cutoff energy<sup>8</sup>.

5. We also computed the parameter,  $r$ , which represents the maximal range of seasonal variations. We found that  $r \approx 20\text{-}25\%$ , from Eq. (39). This result is not very sensitive to our parameters within our simplified treatment of the problem as discussed in the text.

6. The parameter  $r$  describing the seasonal variation remains large for much higher energies, up to 100 keV, as mentioned in item 2. This prediction can be tested in future experiments by any instrument sensitive to energies well above 6 keV.

In this paper, we did not explore all of the possible masses and sizes that nuggets can have. In contrast to the uniform size,  $R$ , and the uniform velocity,  $v_{\text{DMG}}$ , of AQNs used in the present work, the more realistic case is that the AQN size follows a distribution based on percolation theory [25], and the AQN velocity follows a Gaussian distribution [18]. In the future, it would be very desirable to take into consideration these two distributions using full scale Monte Carlo simulations.

Our computations of the spectrum and intensity can be used to plan future experiments which could perform the annual modulation studies in the near-Earth environment as long as they can be done without additional complications related to the changes of the altitude of the telescope and the direction of the field-of-view. On the other hand, the satellite position and orientation can strongly affect the seasonal modulation of the X-ray signal, as we have discussed in Subsection 5.2. Thus, we need to know the exact positions and orientations of XMM-Newton when it made those observations. With the full orbit information implemented into the AQN framework, we may finally fully reproduce the observed pattern in Fig. 1, i.e.  $\text{Fall} > \text{Spring} \approx \text{Summer} > \text{Winter}$ . We leave this for our future work.

Perhaps, the most important aspect of this work is our prediction for near-Earth seasonal variations at higher energies. Indeed, the CXB observed by XMM-Newton was used here to constrain a few parameters of the model, which leads to a deterministic prediction of the signal at higher energies. Such a prediction could provide a decisive test of the AQN model. As shown in this paper, the radiation spectrum extends well beyond 6 keV, and we are in a position to make a prediction in the  $\gamma$ -ray range. In particular, NuSTAR (Nuclear Spectroscopic Telescope Array) is a NASA space based X ray telescope which operates in the range 3 to 79 keV. It would be very desirable<sup>9</sup> if NuSTAR could analyse the seasonal variation in extended energy range up to 79 keV. Essentially this work predicts the spectrum and estimates the intensity in this energy range. Another, possible detector which is capable to test our predictions is the Gamma-ray Burst Monitor (GBM) instrument on the Fermi Telescope which has multi-year archival data of  $\gamma$ -ray background measurements in the near-Earth environment [34]. This would constitute the ideal data set to test our model because we are able to predict uniquely the X-ray background, as seen with XMM-Newton, and the  $\gamma$ -ray background, as seen by GBM. According to the AQN model, the two back-

---

<sup>8</sup>cutoff energy for EPIC pn is  $\sim 15$  keV. However, the authors of [1] do not provide any details for seasonal variations for higher energies above 6 keV.

<sup>9</sup>We thank anonymous Referee for this suggestion.

grounds, separated by two orders of magnitude in frequency, should share very similar properties, once the instrumental and astrophysical sources are removed. This exciting project is left for our future work.

### Acknowledgments

This work was supported by the National Science and Engineering Research Council of Canada.

### Appendix A. Calculations of $dF/d\omega$ and $F_{\text{tot}}$

First, we calculate the spectral surface emissivity (1) with all of the extra effects discussed in Section 3.1 included. Only photons with an energy larger than the plasma frequency,  $\omega_p(z)$ , can propagate outside of the system. The largest plasma frequency,  $\omega_p(z=0)$ , occurs in the deepest region of the electrosphere, where the positron density is the largest. Therefore, photons with an energy,  $\omega > \omega_p(z=0)$ , created anywhere in the electrosphere, ( $z \geq 0$ ), can propagate outside of the system. For  $\omega < \omega_p(z=0)$ , there is a cutoff determined by (10):

$$z_0(\omega) = \frac{1}{\omega} \sqrt{\kappa} \sqrt{\frac{2T}{m_e}} - \bar{z}. \quad (\text{A.1})$$

Photons with an energy,  $\omega < \omega_p(z=0)$ , can propagate outside of the system only if they are created in the regime,  $z > z_0(\omega)$ . Therefore,  $dF/d\omega$  (1) becomes a piecewise function with  $\omega_p(z=0)$  as the turning point.

We should also notice that when  $\omega$  is small enough, the lower cutoff,  $z_0(\omega)$  (A.1), could be larger than the upper cutoff,  $z_1$  (9), defined by the ionization effect. We can then get a critical frequency by equating  $z_0 = z_1$ :

$$\omega_{z_0=z_1}(T) = \sqrt{\kappa} \sqrt{\frac{2T}{m_e}} [z_1(T) + \bar{z}(T)]^{-1}. \quad (\text{A.2})$$

We see that  $z_0 < z_1$  for  $\omega > \omega_{z_0=z_1}$ , while  $z_0 > z_1$  for  $\omega < \omega_{z_0=z_1}$ . Only photons with  $\omega > \omega_{z_0=z_1}$  can be generated. The low frequency photons with  $\omega < \omega_{z_0=z_1}$  cannot be generated because the region of the electrosphere that could generate them is ionized (see Eq. (8)). Therefore,  $dF/d\omega$  should be written as:

$$\frac{dF}{d\omega}(\omega) = \begin{cases} \frac{1}{2} \int_{z_0(\omega)}^{z_1} dz \frac{d\tilde{Q}}{d\omega}(\omega, z), & \text{if } \omega_{z_0=z_1} < \omega < \omega_p(z=0); \\ \frac{1}{2} \int_0^{z_1} dz \frac{d\tilde{Q}}{d\omega}(\omega, z), & \text{if } \omega > \omega_p(z=0). \end{cases} \quad (\text{A.3})$$

Integrating  $d\tilde{Q}/d\omega$  (11) over  $z$  gives:

$$\begin{aligned}
\int dz \frac{d\tilde{Q}}{d\omega}(\omega, z) &= \int dz n^2(z) e^{-\omega_p(z)/T} G(\omega) \\
&= \kappa^2 \left( \frac{T}{2\pi\alpha} \right)^2 G(\omega) \int dz \frac{e^{-\sqrt{\kappa} \sqrt{\frac{2}{m_e T}} \frac{1}{z+\bar{z}}}}{(z+\bar{z})^4} \\
&= \kappa^2 \left( \frac{T}{2\pi\alpha} \right)^2 G(\omega) H(z),
\end{aligned} \tag{A.4}$$

with

$$\begin{aligned}
H(z) &= e^{-\sqrt{\frac{2\kappa}{m_e T}} \frac{1}{z+\bar{z}}} \left[ \frac{1}{\sqrt{\frac{2\kappa}{m_e T}}} \frac{1}{(z+\bar{z})^2} + \frac{2}{\left(\sqrt{\frac{2\kappa}{m_e T}}\right)^2} \frac{1}{(z+\bar{z})} \right. \\
&\quad \left. + \frac{2}{\left(\sqrt{\frac{2\kappa}{m_e T}}\right)^3} \right].
\end{aligned} \tag{A.5}$$

$G(\omega)$  in (A.4) is a function defined for convenience to collect the terms that do not depend on  $z$ :

$$G(\omega) \equiv \frac{4\alpha}{15} \left( \frac{\alpha}{m_e} \right)^2 2\sqrt{\frac{2T}{m_e \pi}} \left( 1 + \frac{\omega}{T} \right) e^{-\omega/T} h\left(\frac{\omega}{T}\right). \tag{A.6}$$

The expression for  $h(x)$  is:

$$h(x) = 17 + 12 \left[ \ln 2 + \left( 1 + e^x \int_1^\infty \frac{e^{-xy}}{y} dy \right) (1+x)^{-1} \right], \tag{A.7}$$

which is a function derived in [27] (we refer the readers to Appendix A2 of [27] for further details). Plugging (A.4) into (A.3), we get:

$$\frac{dF}{d\omega}(\omega) = \begin{cases} \frac{1}{2} \kappa^2 \left( \frac{T}{2\pi\alpha} \right)^2 \cdot G(\omega) \cdot [H(z_1) - H(z_0(\omega))], & \text{if } \omega_{z_0=z_1} < \omega < \omega_p(z=0); \\ \frac{1}{2} \kappa^2 \left( \frac{T}{2\pi\alpha} \right)^2 \cdot G(\omega) \cdot [H(z_1) - H(0)], & \text{if } \omega > \omega_p(z=0). \end{cases} \tag{A.8}$$

We plot  $dF/d\omega$  vs.  $\omega$  in Fig. 2 of the main text for  $\kappa = 10^{-3}$  with  $T = 20$  keV and 50 keV respectively, for illustrative purpose.

Now, we are ready to calculate the total surface emissivity,  $F_{\text{tot}}(T)$ , by integrating

$dF/d\omega$  over  $\omega$ :

$$\begin{aligned}
F_{\text{tot}}(T) &= \int_{\omega_{z_0=z_1}(T)}^{\infty} d\omega \frac{dF}{d\omega}(\omega) \\
&= \left[ \int_{\omega_{z_0=z_1}(T)}^{\omega_p(z=0)} d\omega \frac{1}{2} \int_{z_0(\omega)}^{z_1} dz \frac{dQ}{d\omega}(\omega, z) \right] \\
&\quad + \left[ \int_{\omega_p(z=0)}^{\infty} d\omega \frac{1}{2} \int_0^{z_1} dz \frac{dQ}{d\omega}(\omega, z) \right] \\
&= \frac{\alpha}{15\pi^{5/2}} \frac{T^5}{m_e} \kappa^2 [I_1(T) + I_2(T)],
\end{aligned} \tag{A.9}$$

with

$$\begin{aligned}
I_1(T) &= \frac{1}{T} \sqrt{2} (m_e T)^{-3/2} \\
&\quad \times \int_{\omega_{z_0=z_1}(T)}^{\omega_p(z=0)} d\omega \left(1 + \frac{\omega}{T}\right) e^{-\frac{\omega}{T}} h\left(\frac{\omega}{T}\right) \cdot [H(z_1) - H(z_0(\omega))], \\
I_2(T) &= \frac{1}{T} \sqrt{2} (m_e T)^{-3/2} \\
&\quad \times \int_{\omega_p(z=0)}^{\infty} d\omega \left(1 + \frac{\omega}{T}\right) e^{-\frac{\omega}{T}} h\left(\frac{\omega}{T}\right) \cdot [H(z_1) - H(0)].
\end{aligned} \tag{A.10}$$

The two dimensionless functions  $I_1(T)$  and  $I_2(T)$  can be solved numerically.

In Fig. A.10, we plot  $[I_1(T) + I_2(T)]$  vs.  $T$  in the range  $1 \text{ keV} \leq T \leq 1000 \text{ keV}$ , for  $\kappa = 10^{-2.5}, 10^{-3.5}$  respectively. We see that the two lines of  $[I_1(T) + I_2(T)]$ , with  $\kappa = 10^{-2.5}$  and  $10^{-3.5}$ , almost overlap with each other, and that they are nearly a linear function of  $T$  in the log-log scale. Then, we fit  $[I_1(T) + I_2(T)]$  to a simple function (the red dashed line in Fig. A.10):

$$[I_1(T) + I_2(T)] = c'_1 \left( \frac{T}{10 \text{ keV}} \right)^{c'_2}, \tag{A.11}$$

with the two fitting parameters

$$c'_1 = 4, \quad c'_2 = -0.89. \tag{A.12}$$

This is a good approximation for  $\kappa = 10^{-2.5}, 10^{-3.5}$ . Then, plugging (A.11) and (A.12) into (A.9), we get:

$$F_{\text{tot,fit}}(T) = \frac{\alpha}{15\pi^{5/2}} \frac{T^5}{m_e} \kappa^2 \cdot c'_1 \left( \frac{T}{10 \text{ keV}} \right)^{c'_2}. \tag{A.13}$$

To see how good the fitted result (A.13) is, we plot it together with the exact  $F_{\text{tot}}$  (A.9) in the top subfigure of Fig. A.11 for  $\kappa = 10^{-2.5}, 10^{-3.5}$ . In the bottom subfigure of Fig. A.11, we also plot the relative error  $(F_{\text{tot}} - F_{\text{tot,fit}})/F_{\text{tot}}$ . We see that the relative error is within 10% for  $T \gtrsim 10 \text{ keV}$ .

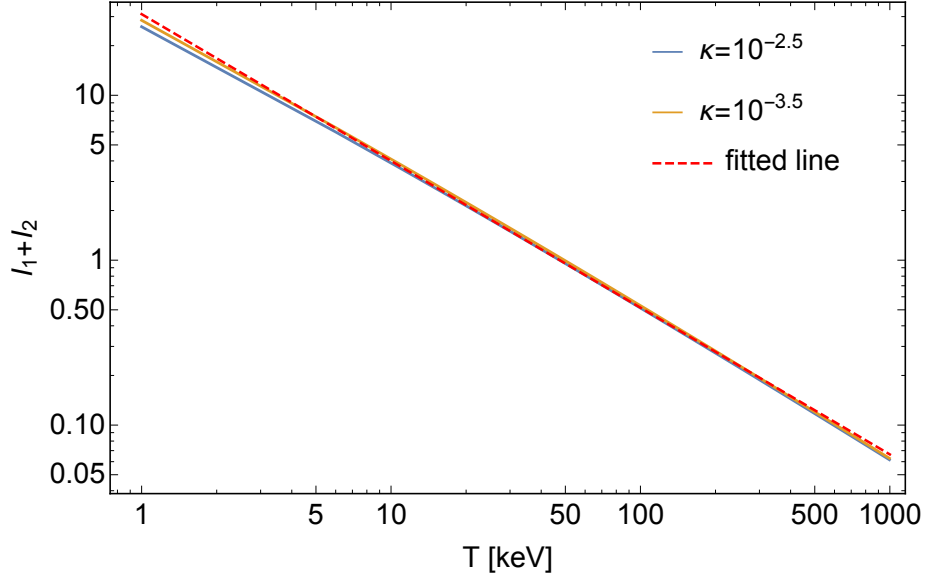


Figure A.10:  $[I_1(T) + I_2(T)]$  as a function of  $T$ , for  $\kappa = 10^{-2.5}, 10^{-3.5}$ . We see that the two lines almost overlap with each other, and that they are fitted to the red dashed line.

## Appendix B. Calculations of nugget cooling

Solving the differential equation (17) gives:

$$\begin{aligned}
 \frac{t}{1 \text{ sec}} &\simeq \frac{R_{\text{AQN}}}{1 \text{ sec}} \frac{5\pi^{5/2}}{3\alpha c_1(\kappa)[c_2(\kappa) + 3]} \frac{m_e(\mu_u^2 + \mu_d^2)}{(10 \text{ keV})^3} \\
 &\cdot \left[ \left( \frac{T}{10 \text{ keV}} \right)^{-[c_2(\kappa)+3]} - \left( \frac{T_0}{10 \text{ keV}} \right)^{-[c_2(\kappa)+3]} \right] \\
 &\simeq \frac{0.34}{c_1(\kappa)[c_2(\kappa) + 3]} \left( \frac{R_{\text{AQN}}}{10^{-5} \text{ cm}} \right) \left( \frac{\mu_{u,d}}{500 \text{ MeV}} \right)^2 \\
 &\cdot \left[ \left( \frac{T}{10 \text{ keV}} \right)^{-[c_2(\kappa)+3]} - \left( \frac{T_0}{10 \text{ keV}} \right)^{-[c_2(\kappa)+3]} \right], \tag{B.1}
 \end{aligned}$$

or equivalently:

$$\begin{aligned}
 T(t) &\simeq 10 \text{ keV} \cdot \left[ \frac{t}{1 \text{ sec}} \left( \frac{R_{\text{AQN}}}{10^{-5} \text{ cm}} \right)^{-1} \left( \frac{\mu_{u,d}}{500 \text{ MeV}} \right)^{-2} \right. \\
 &\cdot \left. \left( \frac{0.34}{c_1(\kappa)[c_2(\kappa) + 3]} \right)^{-1} + \left( \frac{T_0}{10 \text{ keV}} \right)^{-[c_2(\kappa)+3]} \right]^{-\frac{1}{c_2(\kappa)+3}}. \tag{B.2}
 \end{aligned}$$

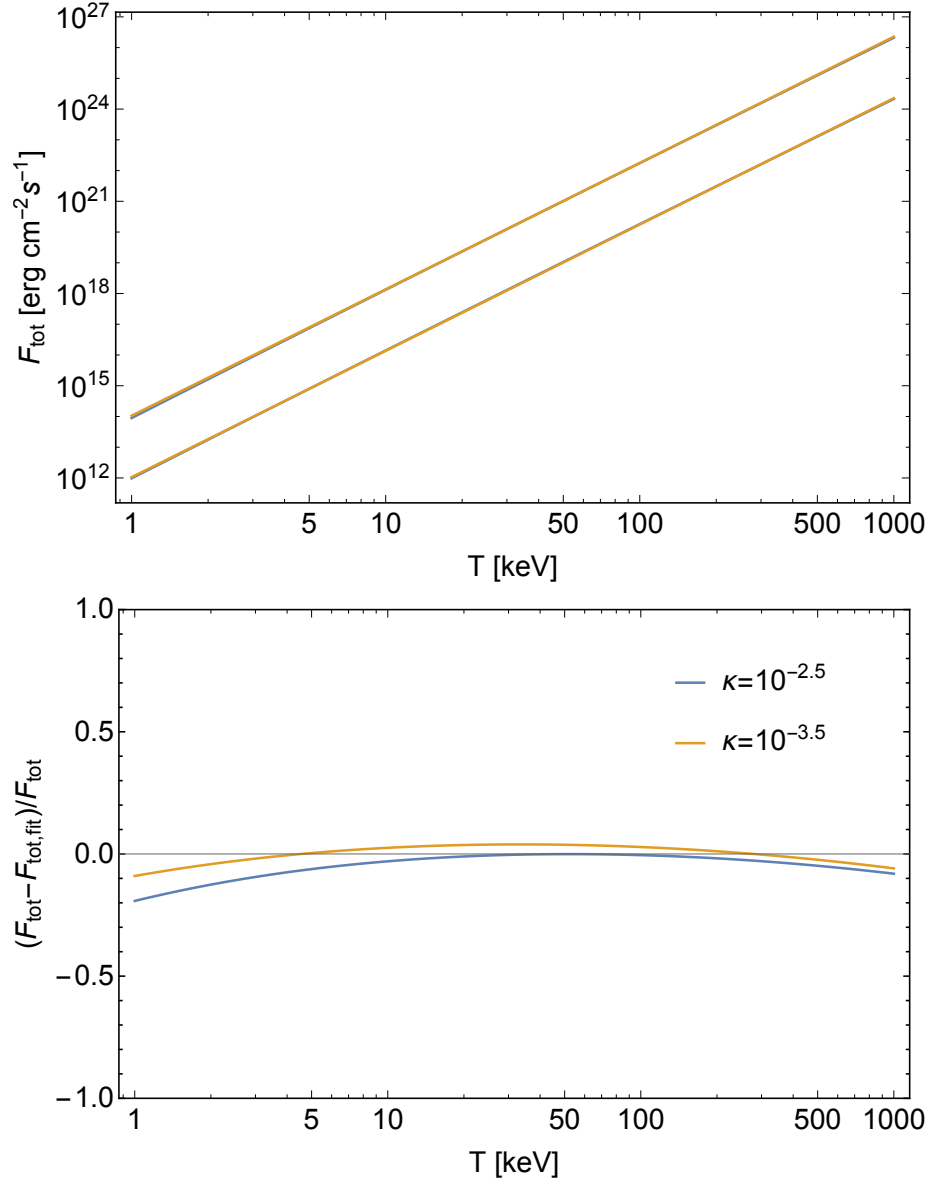


Figure A.11: Top subfigure: the relation  $F_{\text{tot}}$  vs.  $T$ , for  $\kappa = 10^{-2.5}, 10^{-3.5}$  (top and bottom respectively). The blue lines are the exact  $F_{\text{tot}}$  (A.9); the yellow lines are the fitted result (A.13). We see that for each given  $\kappa$ , the blue line almost overlaps with the corresponding yellow line. Bottom subfigure: the relative error.



### Appendix C. Calculations of $dF_r/d\omega$ as a function of $v_{\text{out}}$

In this appendix, we are going to calculate (35) to find the relation between  $dF_r/d\omega$  and  $v_{\text{out}}$ . First, we analyze the factor  $dF/d\omega$  that occurs in (35). The expression of  $dF/d\omega$  is given in (A.8). As we have explained in Section 5 of the main text, we are only interested in the second branch ( $\omega > \omega_p(z=0)$ ) of the piecewise function (A.8).

As we can see from Fig. 3, the nuggets are still very hot when they enter the XMM-Newton's cone. We have  $T \gg \omega$ , where  $\omega \sim 2\text{-}6$  keV is the frequency range that we are interested in. This results in the pattern from the ‘‘soft photon theorem,’’ as explained in Section 4. We can drop the terms suppressed by  $\omega/T$ , so the second branch of (A.8) is approximated as:

$$\frac{dF}{d\omega} \propto T^{5/2} \cdot P(\omega, T), \quad (\text{C.1})$$

where

$$P(\omega, T) \equiv h \left( \frac{\omega}{T} \right) [H(z_1(T), T) - H(0, T)]. \quad (\text{C.2})$$

In Fig. C.12, we plot the relation  $P(\omega, T)$  vs.  $T$ , for  $\kappa = 10^{-2.5}, 10^{-3.5}$ . We see that  $P(\omega, T)$  can be well fitted to the red dashed line, which represents the function [constant  $\times T^{0.72}$ ]. So we have:

$$P(\omega, T) \propto T^{0.72}. \quad (\text{C.3})$$

Note that  $P(\omega, T)$  is also a function of  $\omega$ , which is only contained in  $h(\omega/T)$ . In plotting Fig. C.12,  $\omega$  is chosen to be 3 keV. Since  $\omega/T \ll 1$ , changing the value of  $\omega$  only slightly affects the value of  $P(\omega, T)$ . Thus, to study the relation between  $P(\omega, T)$  and  $T$ , we can fix  $\omega$  at a certain value. This is good enough for our approximate analysis in this appendix. Combining (C.1) and (C.3), we get:

$$\frac{dF}{d\omega} \propto T^{3.22}. \quad (\text{C.4})$$

The relation between  $T$  and  $v_{\text{out}}$  is given in (B.2). We can rewrite (B.2) as:

$$T \simeq 10 \text{ keV} \cdot \left[ \frac{K_1(\kappa)}{v_{\text{out}}} + K_2(\kappa, T_0) \right]^{-\frac{1}{c_2(\kappa)+3}}, \quad (\text{C.5})$$

where

$$\begin{aligned} K_1(\kappa) &\equiv \frac{s}{1 \text{ sec}} \cdot \left( \frac{0.34}{c_1(\kappa)[c_2(\kappa)+3]} \right)^{-1} \left( \frac{R_{\text{AQN}}}{10^{-5} \text{ cm}} \right)^{-1} \\ &\quad \cdot \left( \frac{\mu_{u,d}}{500 \text{ MeV}} \right)^{-2}, \\ K_2(\kappa, T_0) &\equiv \left( \frac{T_0}{10 \text{ keV}} \right)^{-[c_2(\kappa)+3]}. \end{aligned} \quad (\text{C.6})$$

Next, we check on possible variations of the factor,  $n_{\text{AQN}}$ , that occurs in (35). From (20), we know that:

$$n_{\text{AQN}} \propto \frac{\mathcal{F}}{v_{\text{out}}} \propto \frac{\mathcal{F}}{v_{\text{in}}} \frac{v_{\text{in}}}{v_{\text{out}}} \propto \frac{v_{\text{in}}}{v_{\text{out}}} = \gamma^{-1}, \quad (\text{C.7})$$

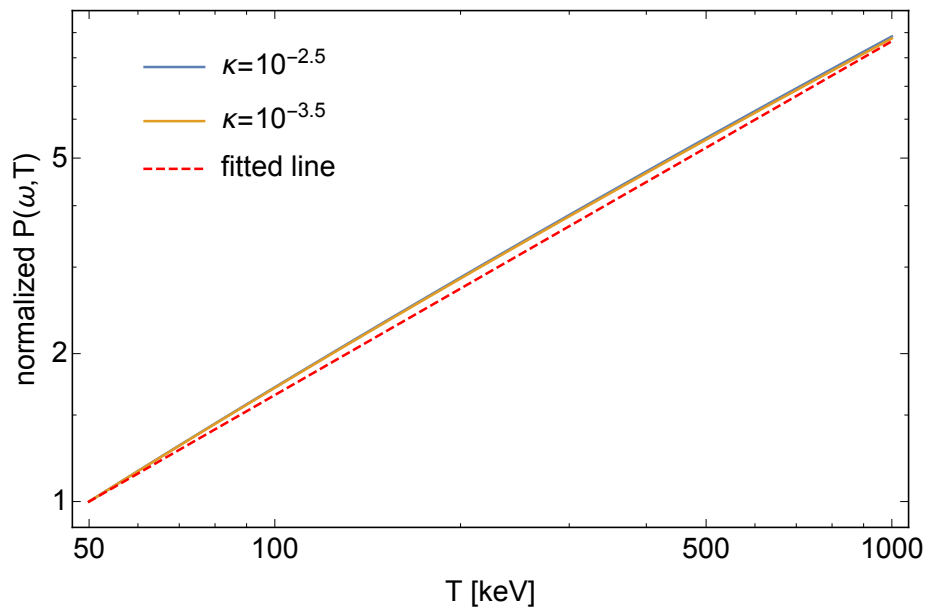


Figure C.12: The relation between the normalized  $P(\omega, T)$  and  $T$ , for  $\kappa = 10^{-2.5}, 10^{-3.5}$ . The two lines almost overlap with each other. We use the function  $[\text{constant} \times T^{0.72}]$  (red dashed line) to fit the two lines. The two lines are plotted at  $\omega = 3$  keV. Changing the value of  $\omega$  only slightly affects the relation between  $P(\omega, T)$  and  $T$ . Since we do not care about the magnitude of  $P(\omega, T)$ , it is actually plotted in the normalized form,  $P(\omega, T)/P(\omega, 50 \text{ keV})$ .

where we have used the relation that  $\mathcal{F}/v_{\text{in}}$  is a constant (see Eq. (21)), and  $\gamma$  is the ratio between  $v_{\text{out}}$  and  $v_{\text{in}}$ , which is defined in Section 5. For simplicity, we assume that the loss of nugget velocity inside the Earth is proportional to the magnitude of the entry velocity,  $v_{\text{in}}$ , so  $\gamma$  and thus  $n_{\text{AQN}}$  are seasonally invariant, despite the fact that  $v_{\text{in}}$  changes with seasons.

Plugging (C.4) and (C.5) into (35), we finally arrive at:

$$\frac{dF_r}{d\omega} \propto \left( \frac{K_1}{v_{\text{out}}} + K_2 \right)^{-\frac{3.22}{c_2(\kappa)+3}}. \quad (\text{C.8})$$

## References

- [1] G. W. Fraser, A. M. Read, S. Sembay, J. A. Carter, E. Schyns, Potential solar axion signatures in X-ray observations with the XMM–Newton observatory, *Mon. Not. Roy. Astron. Soc.* 445 (2) (2014) 2146–2168. [arXiv:1403.2436](#), [doi:10.1093/mnras/stu1865](#).
- [2] L. Di Lella, K. Zioutas, *Astroparticle Physics* 19 (2003) 145. [doi:10.1016/S0370-2693\(02\)01505-8](#).
- [3] H. Davoudiasl, P. Huber, Detecting solar axions using earth’s magnetic field, *Phys. Rev. Lett.* 97 (2006) 141302. [arXiv:hep-ph/0509293](#), [doi:10.1103/PhysRevLett.97.141302](#).
- [4] H. Davoudiasl, P. Huber, Feasibility Study for Measuring Geomagnetic Conversion of Solar Axions to X-rays in Low Earth Orbits, *JCAP* 0808 (2008) 026. [arXiv:0804.3543](#), [doi:10.1088/1475-7516/2008/08/026](#).
- [5] M. Roncadelli, F. Tavecchio, No axions from the Sun, *Mon. Not. Roy. Astron. Soc.* 450 (1) (2015) L26–L28. [arXiv:1411.3297](#), [doi:10.1093/mnrasl/slv040](#).
- [6] D. H. Lumb, R. S. Warwick, M. Page, A. De Luca, X-ray background measurements with xmm-newton epic, *Astron. Astrophys.* 389 (2002) 93. [arXiv:astro-ph/0204147](#), [doi:10.1051/0004-6361:20020531](#).
- [7] A. R. Zhitnitsky, ‘Nonbaryonic’ dark matter as baryonic colour superconductor, *JCAP* 10 (2003) 010. [arXiv:hep-ph/0202161](#), [doi:10.1088/1475-7516/2003/10/010](#).
- [8] V. V. Flambaum, A. R. Zhitnitsky, Primordial Lithium Puzzle and the Axion Quark Nugget Dark Matter Model, *Phys. Rev. D* 99 (2) (2019) 023517. [arXiv:1811.01965](#), [doi:10.1103/PhysRevD.99.023517](#).
- [9] A. Zhitnitsky, Solar Extreme UV radiation and quark nugget dark matter model, *JCAP* 10 (2017) 050. [arXiv:1707.03400](#), [doi:10.1088/1475-7516/2017/10/050](#).

- [10] N. Raza, L. Van Waerbeke, A. Zhitnitsky, Solar Corona Heating by the Axion Quark Nugget Dark Matter, *Phys. Rev. D* 98 (10) (2018) 103527. [arXiv:1805.01897](#), [doi:10.1103/PhysRevD.98.103527](#).
- [11] K. Lawson, A. R. Zhitnitsky, The 21cm Absorption Line and Axion Quark Nugget Dark Matter Model, *Phys. Dark Univ.* 24 (2019) 100295. [arXiv:1804.07340](#), [doi:10.1016/j.dark.2019.100295](#).
- [12] R. Bernabei, et al., Final model independent result of DAMA/LIBRA-phase1, *Eur. Phys. J. C* 73 (2013) 2648. [arXiv:1308.5109](#), [doi:10.1140/epjc/s10052-013-2648-7](#).
- [13] R. Bernabei, et al., No role for neutrons, muons and solar neutrinos in the DAMA annual modulation results, *Eur. Phys. J. C* 74 (12) (2014) 3196. [arXiv:1409.3516](#), [doi:10.1140/epjc/s10052-014-3196-5](#).
- [14] A. Zhitnitsky, DAMA/LIBRA annual modulation and Axion Quark Nugget Dark Matter Model, *Phys. Rev. D* 101 (8) (2020) 083020. [arXiv:1909.05320](#), [doi:10.1103/PhysRevD.101.083020](#).
- [15] D. H. Oaknin, A. R. Zhitnitsky, 511-KeV photons from color superconducting dark matter, *Phys. Rev. Lett.* 94 (2005) 101301. [arXiv:hep-ph/0406146](#), [doi:10.1103/PhysRevLett.94.101301](#).
- [16] A. Zhitnitsky, The Width of the 511-KeV Line from the Bulge of the Galaxy, *Phys. Rev. D* 76 (2007) 103518. [arXiv:astro-ph/0607361](#), [doi:10.1103/PhysRevD.76.103518](#).
- [17] A. Zhitnitsky, The mysterious diffuse UV radiation and axion quark nugget dark matter model, *Phys. Lett. B* 828 (2022) 137015. [arXiv:2110.05489](#), [doi:10.1016/j.physletb.2022.137015](#).
- [18] K. Lawson, X. Liang, A. Mead, M. S. R. Siddiqui, L. Van Waerbeke, A. Zhitnitsky, Gravitationally trapped axions on Earth, *Phys. Rev. D* 100 (4) (2019) 043531. [arXiv:1905.00022](#), [doi:10.1103/PhysRevD.100.043531](#).
- [19] K. Freese, J. A. Frieman, A. Gould, Signal Modulation in Cold Dark Matter Detection, *Phys. Rev. D* 37 (1988) 3388–3405. [doi:10.1103/PhysRevD.37.3388](#).
- [20] K. Freese, M. Lisanti, C. Savage, Colloquium: Annual modulation of dark matter, *Rev. Mod. Phys.* 85 (2013) 1561–1581. [doi:10.1103/RevModPhys.85.1561](#).  
URL <https://link.aps.org/doi/10.1103/RevModPhys.85.1561>
- [21] E. Witten, Cosmic Separation of Phases, *Phys. Rev. D* 30 (1984) 272–285. [doi:10.1103/PhysRevD.30.272](#).

- [22] X. Liang, A. Zhitnitsky, Axion field and the quark nugget's formation at the QCD phase transition, *Phys. Rev. D* 94 (8) (2016) 083502. [arXiv:1606.00435](#), [doi:10.1103/PhysRevD.94.083502](#).
- [23] S. Ge, X. Liang, A. Zhitnitsky, Cosmological C P -odd axion field as the coherent Berry's phase of the Universe, *Phys. Rev. D* 96 (6) (2017) 063514. [arXiv:1702.04354](#), [doi:10.1103/PhysRevD.96.063514](#).
- [24] S. Ge, X. Liang, A. Zhitnitsky, Cosmological axion and a quark nugget dark matter model, *Phys. Rev. D* 97 (4) (2018) 043008. [arXiv:1711.06271](#), [doi:10.1103/PhysRevD.97.043008](#).
- [25] S. Ge, K. Lawson, A. Zhitnitsky, The Axion Quark Nugget Dark Matter Model: Size Distribution and Survival Pattern, *Phys. Rev. D* 99 (2019) 116017. [arXiv:1903.05090](#), [doi:10.1103/PhysRevD.99.116017](#).
- [26] A. Zhitnitsky, Axion quark nuggets. Dark matter and matter–antimatter asymmetry: Theory, observations and future experiments, *Mod. Phys. Lett. A* 36 (18) (2021) 2130017. [arXiv:2105.08719](#), [doi:10.1142/S0217732321300172](#).
- [27] M. M. Forbes, A. R. Zhitnitsky, WMAP Haze: Directly Observing Dark Matter?, *Phys. Rev. D* 78 (2008) 083505. [arXiv:0802.3830](#), [doi:10.1103/PhysRevD.78.083505](#).
- [28] A. Zhitnitsky, The Mysterious Bursts observed by Telescope Array and Axion Quark Nuggets, *J. Phys. G* 48 (6) (2021) 065201. [arXiv:2008.04325](#), [doi:10.1088/1361-6471/abd457](#).
- [29] A. Zhitnitsky, Multi-Modal Clustering Events Observed by Horizon-10T and Axion Quark Nuggets, *Universe* 7 (10) (2021) 384. [arXiv:2108.04826](#), [doi:10.3390/universe7100384](#).
- [30] D. Budker, V. V. Flambaum, A. Zhitnitsky, Infrasonic, acoustic and seismic waves produced by the Axion Quark Nuggets, *Symmetry* 14 (2022) 459. [arXiv:2003.07363](#), [doi:10.3390/sym14030459](#).
- [31] M. G. Alford, A. Schmitt, K. Rajagopal, T. Schafer, Color superconductivity in dense quark matter, *Rev. Mod. Phys.* 80 (2008) 1455–1515. [arXiv:0709.4635](#), [doi:10.1103/RevModPhys.80.1455](#).
- [32] ESA:XMM-NewtonSOC, Xmm-newton users' handbook, Issue 2.17. URL [http://xmm-tools.cosmos.esa.int/external/xmm\\_user\\_support/documentation/uhb/XMM\\_UHB.pdf](http://xmm-tools.cosmos.esa.int/external/xmm_user_support/documentation/uhb/XMM_UHB.pdf)
- [33] M. Santos-Lleó, N. Schartel, M. Guainazzi, P. Rodriguez-Pascual, M. Ehle, M. Breittfellner, L. Tomas, F. Jansen, The life cycle of xmm-newton's targets of opportunity', *ESA Bulletin* 107 (2001) 54–62.

- [34] C. Meegan, G. Lichti, P. N. Bhat, E. Bissaldi, M. S. Briggs, V. Connaughton, R. Diehl, G. Fishman, J. Greiner, A. S. Hoover, A. e. J. van der Horst, A. von Kienlin, R. M. Kippen, C. Kouveliotou, S. McBreen, W. S. Paciesas, R. Preece, H. Steinle, M. S. Wallace, R. B. Wilson, C. Wilson-Hodge, The Fermi Gamma-ray Burst Monitor, *Astrophys. J.* 702 (1) (2009) 791–804. [arXiv:0908.0450](https://arxiv.org/abs/0908.0450), [doi:10.1088/0004-637X/702/1/791](https://doi.org/10.1088/0004-637X/702/1/791).